Energy-stable discretization of the one-dimensional two-fluid model

Buist, J. F.H.; Sanderse, B.; Dubinkina, S.; Oosterlee, C. W.; Henkes, R. A.W.M.

Energy-stable discretization of the one-dimensional two-fluid model

J.F.H. Buist [a,b,*], B. Sanderse [a], S. Dubinkina [c], C.W. Oosterlee [d], R.A.W.M. Henkes [e]

[a] *Scientific Computing Group, Centrum Wiskunde & Informatica (CWI), Amsterdam, The Netherlands*
[b] *Department of Process & Energy, Delft University of Technology, Delft, The Netherlands*
[c] *Department of Mathematics, Vrije Universiteit Amsterdam, Amsterdam, The Netherlands*
[d] *Mathematical Institute, Utrecht University, Utrecht, The Netherlands*
[e] *J.M. Burgerscentrum, Delft University of Technology, Delft, The Netherlands*

ARTICLE INFO

ABSTRACT

In this paper we present a complete framework for the energy-stable simulation of stratified incompressible flow in channels, using the one-dimensional two-fluid model. Building on earlier energy-conserving work on the basic two-fluid model, our new framework includes diffusion, friction, and surface tension. We show that surface tension can be added in an energy-conserving manner, and that diffusion and friction have a strictly dissipative effect on the energy.

We then propose spatial discretizations for these terms such that a semi-discrete model is obtained that has the same conservation properties as the continuous model. Additionally, we propose a new energy-stable advective flux scheme that is energy-conserving in smooth regions of the flow and strictly dissipative where sharp gradients appear. This is obtained by combining, using flux limiters, a previously developed energy-conserving advective flux with a novel first-order upwind scheme that is shown to be strictly dissipative.

The complete framework, with diffusion, surface tension, and a bounded energy, is linearly stable to short wavelength perturbations, and exhibits nonlinear damping near shocks. The model yields smoothly converging numerical solutions, even under conditions for which the basic two-fluid model is ill-posed. With our explicit expressions for the dissipation rates, we are able to attribute the nonlinear damping to the different dissipation mechanisms, and compare their effects.

1. Introduction

The one-dimensional two-fluid model (TFM) is a cross-sectionally averaged model for two-phase flow in pipes and channels. Velocities and phase fractions are resolved only along the main direction of flow, for each fluid separately. This yields an efficient model that is useful when calculations are needed quickly, or when many calculations need to be made. It is most commonly used for flow assurance in oil and gas or CO_2 transport (Aursand et al., 2013; Goldszal et al., 2007), and for safety analysis of steam-water flows in nuclear reactors (Berry et al., 2014). In this paper we consider the incompressible and isothermal form of the TFM. Note that the one-dimensional model discussed in this work, with averages taken over the portions of the pipe or channel cross section occupied by each fluid, differs from multi-dimensional two-fluid models with a local averaging, as described for example by Chahed et al. (2003).

The TFM possesses the ability to dynamically simulate the Kelvin–Helmholtz instability which arises at the interface between two fluids flowing at different velocities. This is a valuable property since it is essential in predicting the transition from stratified flow to slug flow, a type of flow which is typically unwanted due to the large loads it places on the pipe (Fabre, 2003). However, for the basic TFM, when the difference between the two fluids' velocities is large, the instability is unphysically severe. Linear stability analysis shows an unbounded growth rate at short wavelengths, leading to the conclusion that the model is ill-posed (Dinh et al., 2003; Drew and Passman, 1999; Montini, 2011). For the basic model, with only first-order terms, the results of the linear stability analysis can be compared to those of a characteristic analysis: short wavelength unbounded instability implies complex eigenvalues (Ramshaw and Trapp, 1978).

The stability issue is intertwined with a modeling issue. Due to the averaged one-dimensional nature of the TFM, not all small-scale dynamics of the instability can be resolved, and there is uncertainty on how to model their effect on the averaged flow. The TFM implicitly carries the *long wavelength assumption*, implying that the TFM can only accurately model perturbations with a wavelength longer than the fluid

---

* Corresponding author at: Scientific Computing Group, Centrum Wiskunde & Informatica (CWI), Amsterdam, The Netherlands.
E-mail address: jurriaan.buist@gmail.com (J.F.H. Buist).

depth (Holmås et al., 2008; Montini, 2011). It is precisely at the poorly modeled short wavelengths that the catastrophic instability takes place.

The issue has led some researchers to use regularizing terms such as an artificial interfacial pressure force which completely eliminates the instability, for both long and short wavelengths (Bestion, 1990; Evje and Flåtten, 2003; Liou et al., 2006). Others have proposed regularizing terms which only eliminate instability below a desired cut-off wavelength, in the form of artificial diffusion, added both to mass and momentum equations (Bonzanini et al., 2017; Holmås et al., 2008). Finally, researchers strive for stabilization through the systematic inclusion of missing physics (Drew and Passman, 1999; López de Bertodano et al., 2017). One example is the introduction by Song and Ishii (2001) of momentum flux parameters, which are intended to take into account the effect of the non-uniformity of the velocity profile. Montini (2011) showed that these can extend the region of state space for which the TFM is well-posed, but unphysically high parameter values are required to stabilize the model for all relevant flow conditions. Other physical stabilizing effects, such as molecular or turbulent diffusion (in axial direction) (Fullmer et al., 2011) and surface tension (Ramshaw and Trapp, 1978), specifically target the short scales.

Beyond the question of the growth of small perturbations, which is answered by linear stability analysis, lies the question of the growth of large perturbations, for which the full nonlinear behavior of the model must be taken into account (López de Bertodano et al., 2017). For related models, namely the single-layer and two-layer shallow water equations, the mechanical energy acts as an entropy function, and as a nonlinear bound on the solution (Bouchut and Morales de Luna, 2008; Fjordholm et al., 2009; van Reeuwijk, 2011). An energy conservation equation can be derived from the governing (mass and momentum conservation) equations, leading to the conclusion that energy is a secondary conserved quantity of the model, following the terminology of Veldman (2021). Energy-conserving discretization schemes, in which the energy conservation property of the continuous equations is retained, have been designed in order to prevent numerical instability (Gassner et al., 2016; van 't Hof and Veldman, 2012). In previous work (Buist et al., 2022) we showed that the basic TFM satisfies an energy conservation equation like the shallow water equations, and developed an energy-conserving finite volume scheme which satisfies a semi-discrete energy conservation equation.

However, in the presence of shocks, the derivation of the energy conservation equation for the continuous model no longer holds, and energy needs to be dissipated (Jameson, 2008). Whereas for the compressible Euler equations the Rankine–Hugoniot relations prescribe the conservation of energy in shocks, for models like the shallow water equations and the isothermal TFM the Rankine–Hugoniot relations only involve conservation of mass and momentum, since these models do not solve an energy equation. Rather, the TFM must satisfy an energy inequality in the presence of shocks, much like the entropy inequality that holds for the compressible Euler equations. Energy-conserving schemes without dissipation will produce numerical oscillations in the presence of shocks. Therefore energy-stable schemes are designed, by taking an energy-conserving scheme as a baseline, and adding strictly dissipative terms, which can only cause a decrease of the energy (Castro et al., 2013; Fjordholm et al., 2011). These dissipative terms typically take the form of numerical diffusion which is proportional to grid cell size, and preferably dissipate the minimum required amount of energy, and only in the vicinity of shocks, where it is needed.

The TFM requires mechanisms both for dissipation in shocks, and for suppression of the unbounded linear instability. Following the approach of Fullmer et al. (2014b), we achieve these effects through the addition of axial (momentum) diffusion and surface tension. In this work, we fit these effects, along with wall and interface friction, into our energy-consistent framework (Buist et al., 2022). Diffusion and friction are shown to be strictly dissipative, surface tension is shown to be energy-conserving, and we present a spatial discretization of these terms that retains these properties. Importantly, we propose a novel

discretization of the advective flux that is energy stable, with numerical dissipation acting near discontinuities in the solution.

The extended framework possesses bounded linear growth rates (with damping at short wavelengths), and possesses a nonlinear bound on the energy. It possesses multiple mechanisms for dissipation, which can be quantified using explicit expressions for the various dissipation rates. The energy-stable nature of the semi-discrete model, consistent with its continuous counterpart, provides additional fidelity in the accuracy of the numerical solution. The framework yields grid-converged numerical solutions, with well-resolved shocks, for flow states for which the basic TFM is linearly ill-posed.

The analysis of the continuous model is given in Section 2, starting with a review of the basic model and its energy behavior, followed by the results for the extended model, and then a detailed analysis of each term separately. In Section 3, these steps are repeated for the semi-discrete model, with the addition of an analysis of the newly proposed advective flux discretization, showing that it is energy stable. The stability of the TFM is discussed in detail in Section 4, in order to motivate the additions to the basic model. In Section 5, the energy and stability properties predicted by analysis are verified using numerical experiments. We test the capability to model a traveling wave, and a growing wave which develops into a shock, and take a detailed look at the different components of the dissipation near the shock. Our conclusions are given in Section 6.

2. Energy conservation and the continuous two-fluid model

2.1. Governing equations for the basic model

The one-dimensional two-fluid model (TFM) is a cross-sectionally averaged model for two-phase flow in a closed conduit (Ishii and Mishima, 1984; Stewart and Wendroff, 1984). The conduit can take different forms, such as a pipe with a circular cross section, as depicted in Fig. 1, a duct with a rectangular cross section, or (more abstractly) a two-dimensional channel with a cross section of zero width. In all cases, the model can be obtained by defining control volumes for the two fluids separately, which are assumed to be stratified with a sharp interface between them, and setting up integral mass and momentum balances for these control volumes. No energy balance is needed, since the flow is assumed to be isothermal (Munkejord, 2006). Additionally, the flow is assumed to be incompressible. The mass and momentum balances are divided by their length Δs, the limit $\Delta s \to 0$ is taken, and the resulting equations are written in terms of cross-sectionally averaged variables, which are functions only of the streamwise coordinate s and time t. An important assumption made in this process is that the streamwise length scale over which variations in the flow occur must be much larger than the normal length scale over which variations occur; this is known as the long wavelength assumption (Holmås et al., 2008; Montini, 2011). The long wavelength assumption implies that along the normal direction the flow is in hydrostatic balance.

The model, in conservative form, is given by (Buist et al., 2022; Sanderse et al., 2017):

$$\frac{\partial \mathbf{q}}{\partial t} + \frac{\partial \mathbf{f}(\mathbf{q})}{\partial s} + \mathbf{j}(\mathbf{q})\frac{\partial p}{\partial s} = \mathbf{0}, \tag{1}$$

with the conservative variables $\mathbf{q}(s,t)$ representing a mass per unit length or momentum per unit length:

$$\mathbf{q}^T = \begin{bmatrix} q_1 & q_2 & q_3 & q_4 \end{bmatrix}$$
$$= \begin{bmatrix} \rho_U A_U & \rho_L A_L & \rho_U u_U A_U & \rho_L u_L A_L \end{bmatrix}.$$

The conservative variables can be written in terms of the primitive variables, namely the cross-sections A_U and A_L (related to the heights H_U and H_L) which are occupied by the upper and lower fluids respectively, the densities ρ_U and ρ_L of each fluid, and the streamwise (averaged) velocities u_U and u_L. In (1), the fluxes are given by

$$\mathbf{f}(\mathbf{q})^T = \begin{bmatrix} f_1(\mathbf{q}) & f_2(\mathbf{q}) & f_3(\mathbf{q}) & f_4(\mathbf{q}) \end{bmatrix}$$
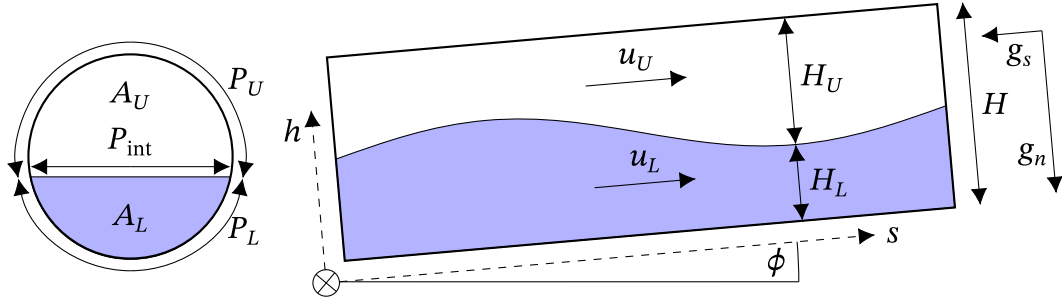
Fig. 1. A schematic of stratified two-fluid flow in ducts (a circular pipe segment is shown as an example) described by the one-dimensional TFM.

$$= \begin{bmatrix} q_3 & q_4 & \dfrac{q_3^2}{q_1} - \rho_U g_n \widehat{H}_U & \dfrac{q_4^2}{q_2} - \rho_L g_n \widehat{H}_L \end{bmatrix}.$$

Here $\widehat{H}_U = \widehat{H}_U(\mathbf{q})$ and $\widehat{H}_L = \widehat{H}_L(\mathbf{q})$ are geometric quantities, defined in Appendix A, which are part of the terms known as the level gradients, which describe the effect of the variation of the hydrostatic pressure along s. The symbol $g_n = g \cos(\phi)$ represents the normal component of gravity, ϕ being the pipe inclination angle.

The pressure p appearing in the equations denotes the pressure at the interface between the two fluids. Its derivative is weighted by the vector $\mathbf{j}$, which is given by

$$\mathbf{j}(\mathbf{q})^T = \begin{bmatrix} 0 & 0 & \dfrac{q_1}{\rho_U} & \dfrac{q_2}{\rho_L} \end{bmatrix}.$$

Since the upper and lower fluid together fill the pipe with cross-section A, the system is subject to the volume constraint

$$\frac{q_1}{\rho_U} + \frac{q_2}{\rho_L} = A,$$

which implies the volumetric flow constraint (Buist et al., 2023)

$$\frac{\partial Q}{\partial s} = 0, \quad \text{with} \quad Q(\mathbf{q}) = \frac{q_3}{\rho_U} + \frac{q_4}{\rho_L} = u_U A_U + u_L A_L. \tag{2}$$

2.2. Energy conservation for the basic model

In this subsection, we give a concise derivation of the energy equation of the basic TFM, based on Buist et al. (2022). The results given in this subsection are not novel, but serve as a necessary basis for the extended energy analysis of later subsections.

The basic TFM has been shown to conserve the following mechanical energy:

$$e_b(\mathbf{q}) = \rho_U g_n \widetilde{H}_U + \rho_L g_n \widetilde{H}_L + \frac{1}{2}\frac{q_3^2}{q_1} + \frac{1}{2}\frac{q_4^2}{q_2}. \tag{3}$$

Here $\widetilde{H}_U = \widetilde{H}_U(A_U(q_1, \rho_U))$ and $\widetilde{H}_L = \widetilde{H}_L(A_L(q_2, \rho_L))$ are geometric terms representing the centers of mass of the upper and lower fluids respectively (see Appendix A). Given a mechanical energy $e_b(\mathbf{q})$, we can define the following vector:

$$\mathbf{v}_b(\mathbf{q})^T := \left[\frac{\partial e_b}{\partial \mathbf{q}} \right] = \begin{bmatrix} -\frac{1}{2}\frac{q_3^2}{q_1^2} + g_n\frac{\mathrm{d}\widetilde{H}_U}{\mathrm{d}A_U} & -\frac{1}{2}\frac{q_4^2}{q_2^2} + g_n\frac{\mathrm{d}\widetilde{H}_L}{\mathrm{d}A_L} & \frac{q_3}{q_1} & \frac{q_4}{q_2} \end{bmatrix}. \tag{4}$$

Taking the dot product of this vector with the governing equations given by (1) yields

$$\left\langle \mathbf{v}_b, \frac{\partial \mathbf{q}}{\partial t} \right\rangle + \left\langle \mathbf{v}_b, \frac{\partial \mathbf{f}}{\partial s} \right\rangle + \left\langle \mathbf{v}_b, \mathbf{j}\frac{\partial p}{\partial s} \right\rangle = 0. \tag{5}$$

Using the geometric relations (A.6), the volumetric flow constraint (2), and assuming g_n to be constant along s, it can be shown that these terms can be written in conservative form (Buist et al., 2022):

$$\left\langle \mathbf{v}_b, \frac{\partial \mathbf{q}}{\partial t} \right\rangle = \frac{\partial e_b}{\partial t}, \quad \left\langle \mathbf{v}_b, \frac{\partial \mathbf{f}}{\partial s} \right\rangle = \frac{\partial h_f}{\partial s}, \quad \left\langle \mathbf{v}_b, \mathbf{j}\frac{\partial p}{\partial s} \right\rangle = \frac{\partial h_p}{\partial s},$$

with

$$h_f = g_n q_3 \frac{\mathrm{d}\widetilde{H}_U}{\mathrm{d}A_U} + g_n q_4 \frac{\mathrm{d}\widetilde{H}_L}{\mathrm{d}A_L} + \frac{1}{2}\frac{q_3^3}{q_1^2} + \frac{1}{2}\frac{q_4^3}{q_2^2}, \tag{6}$$

and

$$h_p = Qp. \tag{7}$$

In the upcoming energy analysis of the additional model terms, we will follow the same structure, and use the insight that the dot product of $\mathbf{v}_b$ with the additional model term yields its contribution to the energy equation.

Since each term in (5) can be written in conservative form, it reduces to the local energy conservation equation

$$\frac{\partial e_b}{\partial t} + \frac{\partial h_b}{\partial s} = 0, \tag{8}$$

with $h_b = h_f + h_p$, which describes how the energy $e_b(s,t)$ at a specific point in space changes due to an inflow or outflow. In case of periodic or closed boundaries, integrating this equation over a section of pipe yields the global energy conservation equation

$$\frac{\mathrm{d}E_b}{\mathrm{d}t} = -\left[h_b \right]_{s_1}^{s_2} = 0, \quad \text{with} \quad E_b(t) = \int_{s_1}^{s_2} e_b \, \mathrm{d}s. \tag{9}$$

This shows that the mechanical energy is a secondary conserved quantity of the TFM (in contrast to the primary conserved quantities of mass and momentum).

2.3. Energy equation for the extended model

Having set up the basic TFM and its energy conservation equation, we will extend it in an energy-consistent manner, with three additions that make it linearly well-posed and energy stable. We will show, in the following subsections, that friction and diffusion have a strictly dissipative effect, while surface tension can be added in an energy-conserving manner. In previous work (Buist et al., 2023), the energy-conserving nature of streamwise gravity and the energy input due to a driving pressure gradient have been demonstrated.

The model, extended with all the additional terms, is given by

$$\boxed{\frac{\partial \mathbf{q}}{\partial t} + \frac{\partial \mathbf{f}}{\partial s} + \mathbf{j}\frac{\partial p}{\partial s} = \frac{\partial \mathbf{d}}{\partial s} + \mathbf{s} + \mathbf{c}_g + \mathbf{c}_f + \mathbf{c}_p} \tag{10}$$

with $\partial \mathbf{d}/\partial s$ representing diffusion, $\mathbf{c}_f$ representing friction, and $\mathbf{s}$ representing surface tension. The expressions for these terms will be given in (16), (20), and (25), respectively. The extended model includes the following contributions from streamwise gravity, indicated in Fig. 1 with $g_s = g \sin(\phi)$:

$$\mathbf{c}_g^T = \begin{bmatrix} 0 & 0 & -g\sin(\phi)q_1 & -g\sin(\phi)q_2 \end{bmatrix},$$

and from a constant driving pressure gradient, which can be applied in cases with periodic boundary conditions in order to balance against streamwise gravity and friction:

$$\mathbf{c}_p^T = \begin{bmatrix} 0 & 0 & -\dfrac{q_1}{\rho_U}\dfrac{\partial p_{\text{body}}}{\partial s} & -\dfrac{q_2}{\rho_L}\dfrac{\partial p_{\text{body}}}{\partial s} \end{bmatrix}.$$

The driving pressure gradient acts as a body force, and is independent of the variable pressure p which acts to make the flow satisfy the volume and volumetric flow constraints.

For the extended model given by (10), the following energy conservation equation will be derived:

$$\frac{\partial e}{\partial t} + \frac{\partial h}{\partial s} = -\epsilon + c_p \tag{11}$$

with

$$e = e_b + e_g + e_\sigma, \tag{12}$$

$$h = h_b + h_g + h_d + h_\sigma, \tag{13}$$

$$\epsilon = \epsilon_d + \epsilon_f. \tag{14}$$

Eq. (11) is the first main novel result of this work. It shows that the mechanical energy e, which consists of kinetic, potential, and surface energy, is locally conserved except for the dissipating effects of diffusion and friction. The upcoming subsections will give the expressions (18) for h_d, (19) for ϵ_d, (23) for ϵ_f, (31a) for e_σ, and (31c) for h_σ. Contributions from streamwise gravity are present in the energy and the energy flux (Buist et al., 2023):

$$e_g = gy(q_1 + q_2), \quad h_g = gy(q_3 + q_4), \quad \text{with} \quad \frac{dy}{ds} = \sin(\phi(s)),$$

while the driving pressure gradient adds a source term:

$$c_p = -Q\frac{\partial p_{\text{body}}}{\partial s},$$

which is strictly positive in a flow which is aligned with its driving pressure gradient, e.g. $Q > 0$ and $\partial p_{\text{body}}/\partial s < 0$. This term differs from the others in that it represents an externally applied force, and therefore does not adhere to the strictly dissipative behavior of the flow itself.

Upon integrating the local energy equation over a periodic domain, the conservative term $\partial h/\partial s$ in (11) vanishes. Besides conservative terms, the new energy equation has an explicit sink term $-\epsilon$ which remains present in the global energy equation:

$$\frac{dE}{dt} = -\mathcal{E} + C_p \quad \text{with} \quad E(t) = \int_{s_1}^{s_2} e\,ds, \quad \mathcal{E} = \int_{s_1}^{s_2} \epsilon\,ds, \tag{15}$$

$$C_p = \int_{s_1}^{s_2} c_p\,ds = -Q\frac{\partial p_{\text{body}}}{\partial s}L,$$

with $L = s_2 - s_1$ the length of the domain. Disregarding the (optional) externally supplied energy source, the energy-conserving basic model has been supplemented with a sink term which will shown to be strictly negative, leading to the dissipation of energy, and an energy-stable model.

Each addition to the model independently results in additional terms in the energy equation. The combined result of all these additions was given here. In the following subsections, the novel terms in (11) will be derived separately.

2.4. Physical diffusion

Our first novel contribution in the continuous setting is that we show that adding viscous diffusion terms to the TFM has a strictly dissipative effect, which can be quantified using an expression for the dissipation rate. We refer to these viscous terms as "physical diffusion" in contrast to the artificial diffusion of Bonzanini et al. (2017), Fullmer et al. (2014a) and Holmås et al. (2008), and the numerical diffusion which will be discussed in Section 3. The physical diffusion terms naturally appear in the derivation of the model, but are typically neglected due to the long wavelength assumption, with the argument that the TFM cannot accurately resolve the scale at which these terms act. However, they are important in bounding the linear instability of short wavelength perturbations (see Section 4), and in bounding nonlinear shocks through dissipation (see Section 5.4).

In the TFM, physical diffusion takes the form of the term $\partial \mathbf{d}/\partial s$ as included in (10), with $\mathbf{d}$ given by (Fullmer et al., 2014b; Montini, 2011)

$$\mathbf{d}^T = \begin{bmatrix} 0 & 0 & v_{\text{eff},U}q_1\frac{\partial}{\partial s}\frac{q_3}{q_1} & v_{\text{eff},L}q_2\frac{\partial}{\partial s}\frac{q_4}{q_2} \end{bmatrix}. \tag{16}$$

We use the effective viscosity model of Fullmer et al. (2011), which combines the material viscosity v_m with a turbulent viscosity v_t. This serves as a closure term for small scale fluctuations that are not resolved by the model:

$$v_{\text{eff}} = C_\epsilon(v_m + v_t),$$

with C_ϵ an adjustment factor. The parameters v_t and C_ϵ are empirical: they can be based on fully resolved (higher dimensional) simulations, specific to a given test case. Physical diffusion conserves momentum, since it can be written in conservative form.

We now consider the effect of physical diffusion on the energy. Unlike the addition of streamwise gravity, the addition of diffusion does not change the energy definition. There is a contribution of the extra terms to the left hand side (LHS) of the energy equation, which is given by

$$-\langle \mathbf{v}_b, \frac{\partial \mathbf{d}}{\partial s} \rangle,$$

with $\mathbf{v}_b$ given by (4). Some manipulation yields (for smooth solutions)

$$-\langle \mathbf{v}_b, \frac{\partial \mathbf{d}}{\partial s} \rangle = -\frac{q_3}{q_1}\frac{\partial}{\partial s}\left(v_{\text{eff},U}q_1\frac{\partial}{\partial s}\frac{q_3}{q_1}\right) - \frac{q_4}{q_2}\frac{\partial}{\partial s}\left(v_{\text{eff},L}q_2\frac{\partial}{\partial s}\frac{q_4}{q_2}\right)$$
$$= \frac{\partial h_d}{\partial s} + \epsilon_d, \tag{17}$$

with

$$h_d = -v_{\text{eff},U}q_1\frac{1}{2}\frac{\partial}{\partial s}\frac{q_3^2}{q_1^2} - v_{\text{eff},L}q_2\frac{1}{2}\frac{\partial}{\partial s}\frac{q_4^2}{q_2^2}, \tag{18}$$

$$\epsilon_d = v_{\text{eff},U}q_1\left(\frac{\partial}{\partial s}\frac{q_3}{q_1}\right)^2 + v_{\text{eff},L}q_2\left(\frac{\partial}{\partial s}\frac{q_4}{q_2}\right)^2. \tag{19}$$

The terms included in the energy flux h_d are energy-conserving, since they can be written in conservative form. The remaining terms, collected in ϵ_d, are not conservative. They are strictly positive, since $v_{\text{eff},U}$, q_1, $v_{\text{eff},L}$, and q_2 must be positive, and the square of the differential terms must be positive. Therefore, when moved to the right hand side (RHS), it becomes clear that $-\epsilon_d$ is a strictly negative sink term. In conclusion, we have proven analytically that physical diffusion leads to dissipation of the energy given by (12), with dissipation rate ϵ_d.

2.5. Friction terms

Our second novel contribution in the continuous setting is that we prove that wall and interface friction add a strictly dissipative sink term to the energy equation. The friction term $\mathbf{c}_f$ can be added to the model as in (10), with

$$\mathbf{c}_f^T = \begin{bmatrix} 0 & 0 & \tau_U P_U + \tau_{\text{int}} P_{\text{int}} & \tau_L P_L - \tau_{\text{int}} P_{\text{int}} \end{bmatrix}. \tag{20}$$

The wall stresses τ_U and τ_L represent the shear stresses acting at the pipe perimeters P_U and P_L, that are in contact with the upper and lower fluids, respectively. The interface stress τ_{int} represents the shear stress at the interface P_{int} between the two fluids. The stress terms in the model are the averaged effect of local stresses on the averaged flow, and in order to express these in terms of the averaged variables, closure relations are required. These typically take the following form (Taitel and Dukler, 1976):

$$\tau_L = -\frac{1}{2}f_L\rho_L u_L|u_L|, \quad \tau_U = -\frac{1}{2}f_U\rho_U u_U|u_U|,$$
$$\tau_{\text{int}} = -\frac{1}{2}f_{\text{int}}\rho_U(u_U - u_L)|u_U - u_L|, \tag{21}$$

in which f_L, f_U, and f_{int} are friction factors that require further closure relations, which are functions of the solution $\mathbf{q}$ (see Appendix B).

We now consider the effect of wall and interface friction on the energy. The contribution of the extra terms to the RHS of the energy equation is

$$+\langle \mathbf{v}_b, \mathbf{c}_f \rangle,$$

with $\mathbf{v}_b$ given by (4). Carrying out the multiplication, substituting (21), and some rewriting yields

$$\langle \mathbf{v}_b, \mathbf{c}_f \rangle = \frac{q_3}{q_1} \left(\tau_U P_U + \tau_{\text{int}} P_{\text{int}} \right) + \frac{q_4}{q_2} \left(\tau_L P_L - \tau_{\text{int}} P_{\text{int}} \right) = -\epsilon_f, \tag{22}$$

with

$$\epsilon_f = \frac{1}{2} f_U \rho_U \left(\frac{q_3}{q_1} \right)^2 \left| \frac{q_3}{q_1} \right| P_U + \frac{1}{2} f_L \rho_L \left(\frac{q_4}{q_2} \right)^2 \left| \frac{q_4}{q_2} \right| P_L$$
$$+ \frac{1}{2} f_{\text{int}} \rho_U \left(\frac{q_3}{q_1} - \frac{q_4}{q_2} \right)^2 \left| \frac{q_3}{q_1} - \frac{q_4}{q_2} \right| P_{\text{int}}. \tag{23}$$

Since f_U, f_L, f_{int}, ρ_U, ρ_L, P_U, P_L, and P_{int} must be positive, and the rest of the terms are either quadratic or absolute, all three terms in (23) must be positive. Therefore, $-\epsilon_f$ will act as a sink in the energy equation, which represents the dissipation of energy due to friction. In conclusion, we have proven analytically that wall and interface friction have a strictly dissipative effect on the energy given by (12).

2.6. Surface tension

Our third novel contribution in the continuous setting is that we show that surface tension can be added to the TFM in such a way that the total energy is conserved. Surface tension is an important addition since it makes the model linearly well-posed (see Section 4). However, if surface tension were to be added in a non-conservative manner, it would spoil the energy-stable nature of the model. Therefore, it is key to find an energy-conserving form of the surface tension.

The effect of surface tension in the TFM is typically modeled through its effect on the pressure. This effect is to introduce a discontinuity in the pressure at the interface. The pressure difference is given by (Montini, 2011; Ramshaw and Trapp, 1978)

$$\Delta p = -\sigma \kappa = \sigma \frac{\partial^2 H_L}{\partial s^2} \left[1 + \left(\frac{\partial H_L}{\partial s} \right)^2 \right]^{-3/2}, \tag{24}$$

with σ the surface tension and κ the streamwise curvature of the interface, with the interface assumed flat along the other direction. This is the Young–Laplace equation for the TFM.

Similar to Fullmer et al. (2014b), we include the effect of this pressure difference through the term $\mathbf{s}$ in (10), with

$$\mathbf{s}^T = \begin{bmatrix} 0 & 0 & 0 & \frac{q_2}{\rho_L} \frac{\partial \Delta p}{\partial s} \end{bmatrix}. \tag{25}$$

This is a general way to write the surface tension. Typically in literature (Barnea and Taitel, 1994; Fullmer et al., 2014b; Montini, 2011; Ramshaw and Trapp, 1978), the assumption $\left(\partial H_L / \partial s \right)^2 \ll 1$ will be made to approximate (24) as:

$$\Delta p \approx \sigma \frac{\partial^2 H_L}{\partial s^2} \approx \frac{\sigma}{P_{\text{int}}} \frac{\partial^2 A_L}{\partial s^2}. \tag{26}$$

Note that for the specific case of a 2D channel geometry ($P_{\text{int}} = 1$, $A_L = H_L$), the two approximations in (26) are equivalent.

We note that, unlike the basic model, surface tension of the form given by (25) is not momentum-conserving, as it cannot be written in conservative form. This is caused by the one-dimensional nature of the model and stands in contrast to higher-dimensional, unaveraged models, where surface tension does conserve momentum (Remmerswaal, 2023).

Though (25) is not momentum-conserving, it can still be energy-conserving, and we aim to find a set of expressions for Δp and the surface energy such that the contribution of surface tension to the energy conservation equation is of conservative form. Physically, the surface tension is associated with an energy, proportional to the surface area, that is conserved in combination with the mechanical energy (Remmerswaal, 2023). The surface area in the one-dimensional two-fluid model (see Fig. 1) will depend on $\partial H_L / \partial s = P_{\text{int}}^{-1} \partial A_L / \partial s$, and P_{int}. Therefore, we introduce the following general form for the surface energy:

$$e_\sigma = e_\sigma(S_{\text{int}}, P_{\text{int}}), \quad \text{with} \quad S_{\text{int}} = \frac{\partial A_L}{\partial s}, \tag{27}$$

with the functional dependencies specified as

$$q_2 = q_2(A_L), \quad P_{\text{int}} = P_{\text{int}}(A_L), \quad S_{\text{int}} = S_{\text{int}}(s, t), \quad A_L = A_L(s, t).$$

The additional term on the LHS of the energy equation due to surface tension as given by (25) is

$$-\langle \mathbf{v}_b, \mathbf{s} \rangle = -\frac{q_4}{\rho_L} \frac{\partial \Delta p}{\partial s}.$$

In order for the model addition to be energy-conserving, the following condition must hold:

$$-\frac{q_4}{\rho_L} \frac{\partial \Delta p}{\partial s} = \frac{\partial h_\sigma}{\partial s} + \frac{\partial e_\sigma}{\partial t}, \tag{28}$$

for in this case the addition to the energy equation will be of conservative form. We will now derive a relation between Δp and e_σ such that (28) holds.

The time derivative of the energy given by (27) is defined by

$$\frac{\partial e_\sigma}{\partial t} = \frac{\partial e_\sigma}{\partial S_{\text{int}}} \frac{\partial S_{\text{int}}}{\partial t} + \frac{\partial e_\sigma}{\partial P_{\text{int}}} \frac{\partial P_{\text{int}}}{\partial t},$$

and under the assumption of smooth solutions, and through substitution of the mass conservation equation for the lower fluid (the second equation of (1)), can be rewritten in the following manner:

$$\frac{\partial e_\sigma}{\partial t} = \frac{\partial e_\sigma}{\partial S_{\text{int}}} \frac{\partial}{\partial s} \left(\rho_L^{-1} \frac{\partial q_2}{\partial t} \right) + \frac{\partial e_\sigma}{\partial P_{\text{int}}} \frac{\mathrm{d} P_{\text{int}}}{\mathrm{d} A_L} \rho_L^{-1} \frac{\partial q_2}{\partial t}$$
$$= -\frac{\partial e_\sigma}{\partial S_{\text{int}}} \frac{\partial}{\partial s} \left(\rho_L^{-1} \frac{\partial q_4}{\partial s} \right) - \frac{\partial e_\sigma}{\partial P_{\text{int}}} \frac{\mathrm{d} P_{\text{int}}}{\mathrm{d} A_L} \rho_L^{-1} \frac{\partial q_4}{\partial s}$$
$$= -\frac{\partial h_\sigma}{\partial s} - \frac{q_4}{\rho_L} \frac{\partial \Delta p}{\partial s},$$

with

$$h_\sigma = \frac{1}{\rho_L} \left(\frac{\partial e_\sigma}{\partial S_{\text{int}}} \frac{\partial q_4}{\partial s} - q_4 \frac{\partial}{\partial s} \left(\frac{\partial e_\sigma}{\partial S_{\text{int}}} \right) + q_4 \frac{\partial e_\sigma}{\partial P_{\text{int}}} \frac{\mathrm{d} P_{\text{int}}}{\mathrm{d} A_L} \right),$$

and

$$\Delta p = \frac{\partial}{\partial s} \left(\frac{\partial e_\sigma}{\partial S_{\text{int}}} \right) - \frac{\partial e_\sigma}{\partial P_{\text{int}}} \frac{\mathrm{d} P_{\text{int}}}{\mathrm{d} A_L}. \tag{29}$$

For an energy of the general form (27), and a surface tension of the general form (25), (29) is the relation between the specific forms of Δp and e_σ, that needs to be satisfied in order to achieve energy conservation.

We now must find a set of expressions for Δp and e_σ, that – first – satisfies (29) and – second – makes physical sense. The most straightforward way to do this is to propose an energy based on physical considerations, substitute this in (29), and check if the resulting expression for Δp compares to our expectation, which is that it take a form similar to (24) or (26). From a physical point of view, the energy should be given by σ times the surface area, which can be expressed as

$$e_\sigma \left(S_{\text{int}}, P_{\text{int}} \right) = \sigma P_{\text{int}} \sqrt{1 + \left(\frac{\partial H_L}{\partial s} \right)^2} = \sigma P_{\text{int}} \sqrt{1 + \left(P_{\text{int}}^{-1} \frac{\partial A_L}{\partial s} \right)^2}$$
$$= \sigma P_{\text{int}} \sqrt{1 + \left(P_{\text{int}}^{-1} S_{\text{int}} \right)^2}.$$

However, substituting this in (29) yields an expression for Δp that does not relate to (24) or (26), and therefore cannot be physically justified. Mimicking the conventional approach of taking approximations such as (26), we take the second order Taylor expansion of this energy around $S_{\text{int}} = 0$:

$$e_\sigma \left(S_{\text{int}}, P_{\text{int}} \right) \approx \sigma \left(P_{\text{int}} + \frac{1}{2} P_{\text{int}}^{-1} S_{\text{int}}^2 \right).$$

Substituting this energy in (29) yields the following expression for Δp:

$$\Delta p_{\text{int}} = \frac{\sigma}{P_{\text{int}}} \frac{\partial S_{\text{int}}}{\partial s} - \sigma \left(1 + \frac{1}{2} P_{\text{int}}^{-2} S_{\text{int}}^2 \right) \frac{\mathrm{d} P_{\text{int}}}{\mathrm{d} A_L}, \tag{30}$$

of which the first term can be recognized in (26), but the second term cannot.

When the scope is reduced from arbitrary geometries to the specific case of the 2D channel geometry, for which $P_{int} = 1$ and $A_L = H_L$, (30) does match (26) exactly. This means that for the channel geometry, the combination

$$e_\sigma = \sigma \left(1 + \frac{1}{2} \left(\frac{\partial H_L}{\partial s} \right)^2 \right), \tag{31a}$$

$$\Delta p = \sigma \frac{\partial^2 H_L}{\partial s^2}, \quad \text{with} \tag{31b}$$

$$h_\sigma = \frac{\sigma}{\rho_L} \left(\frac{\partial q_4}{\partial s} \frac{\partial H_L}{\partial s} - q_4 \frac{\partial^2 H_L}{\partial s^2} \right), \tag{31c}$$

is energy-conserving, and it can be justified physically, since e_σ is an approximation of σ times the surface area, and Δp is an approximation of the Young–Laplace equation. This expression for Δp can be substituted in (25) to obtain an energy-conserving form of the surface tension.

We have therefore found a form of the surface tension **s**, and an associated surface energy e_σ, with which the basic model can be extended, while retaining its energy-conserving behavior. For the 2D channel geometry, this turned out to be equivalent to a standard form, often used in literature.

3. Energy conservation and the semi-discrete two-fluid model

3.1. Semi-discrete equations for the basic model

With the energy analysis for the continuous model complete, we will continue to propose a discretization that inherits the energy properties of the three additions to the model on the discrete level. In order to obtain the same conservation properties for the discrete model as for the continuous model, the model must be discretized in a specific manner. Therefore, the energy analysis guides the discretization. In this subsection, we will first summarize the previously found energy-conserving discretization of the basic model (Buist et al., 2022), to which energy-consistent discretizations of the additional model terms will be added.

We define the unknowns of the semi-discrete TFM on a staggered grid, depicted in Fig. 2, in the following manner:

$$\mathbf{q}_i(t) := \begin{bmatrix} q_{1,i}(t) \\ q_{2,i}(t) \\ q_{3,i-1/2}(t) \\ q_{4,i-1/2}(t) \end{bmatrix} = \begin{bmatrix} (\rho_U A_U \Delta s)_i \\ (\rho_L A_L \Delta s)_i \\ (\rho_U A_U u_U \Delta s)_{i-1/2} \\ (\rho_L A_L u_L \Delta s)_{i-1/2} \end{bmatrix}, \tag{32}$$

We introduce the following notation to denote central interpolation and jumps respectively:

$$\bar{a}_{i-1/2} := \frac{1}{2} (a_{i-1} + a_i), \quad \bar{a}_i := \frac{1}{2} (a_{i-1/2} + a_{i+1/2}), \tag{33}$$

$$[\![a_{i-1/2}]\!] := a_i - a_{i-1}, \quad [\![a_i]\!] := a_{i+1/2} - a_{i-1/2}. \tag{34}$$

The primitive variables can be extracted from (32) through the following relations:

$$A_{U,i} = \frac{q_{1,i}}{\rho_U \Delta s}, \quad A_{L,i} = \frac{q_{2,i}}{\rho_L \Delta s}, \quad u_{U,i-1/2} = \frac{q_{3,i-1/2}}{\bar{q}_{1,i-1/2}}, \quad u_{L,i-1/2} = \frac{q_{4,i-1/2}}{\bar{q}_{2,i-1/2}}. \tag{35}$$

With this notation, the semi-discrete finite volume scheme can be written locally as

$$\frac{d\mathbf{q}_i}{dt} + [\![\mathbf{f}_i]\!] + \mathbf{j}_i [\![p_{i-1/2}]\!] = \mathbf{0}, \tag{36}$$

with

$$\mathbf{f}_{i-1/2} := \begin{bmatrix} f_{1,i-1/2} \\ f_{2,i-1/2} \\ f_{3,i-1} \\ f_{4,i-1} \end{bmatrix} = \begin{bmatrix} \frac{q_{3,i-1/2}}{\Delta s} \\ \frac{q_{4,i-1/2}}{\Delta s} \\ \overline{\left(\frac{q_{3,i}}{\bar{q}_{1,i}} \right) \bar{q}_{3,i-1}} \frac{1}{\Delta s} - \rho_U g_n \hat{H}_{U,i-1} \\ \overline{\left(\frac{q_{4,i}}{\bar{q}_{2,i}} \right) \bar{q}_{4,i-1}} \frac{1}{\Delta s} - \rho_L g_n \hat{H}_{L,i-1} \end{bmatrix}, \quad \text{and} \tag{37a}$$

$$\mathbf{j}_i := \begin{bmatrix} j_{1,i} \\ j_{2,i} \\ j_{3,i-1/2} \\ j_{4,i-1/2} \end{bmatrix} = \begin{bmatrix} 0 \\ 0 \\ \frac{\bar{q}_{1,i-1/2}}{\rho_U \Delta s} \\ \frac{\bar{q}_{2,i-1/2}}{\rho_L \Delta s} \end{bmatrix}. \tag{37b}$$

The semi-discrete version of the volume constraint is given by

$$\frac{q_{1,i}}{\rho_U \Delta s} + \frac{q_{2,i}}{\rho_L \Delta s} = A,$$

which implies the volumetric flow constraint (Buist et al., 2023)

$$[\![Q_i]\!] = 0, \quad \text{with} \quad Q_{i-1/2}(\mathbf{q}_i) := \frac{q_{3,i-1/2}}{\rho_U \Delta s} + \frac{q_{4,i-1/2}}{\rho_L \Delta s}. \tag{38}$$

3.2. Energy conservation for the semi-discrete basic model

The basic TFM, discretized as given above, conserves the following discretized mechanical energy:

$$e_{b,i-1/2} = \rho_U g_n \overline{\tilde{H}}_{U,i-1/2} \Delta s + \rho_L g_n \overline{\tilde{H}}_{L,i-1/2} \Delta s + \frac{1}{2} \frac{q_{3,i-1/2}^2}{\bar{q}_{1,i-1/2}} + \frac{1}{2} \frac{q_{4,i-1/2}^2}{\bar{q}_{2,i-1/2}}. \tag{39}$$

This result was obtained in Buist et al. (2022). Here we will give a concise version of the proof. This is needed as a basis for the extensions of the semi-discrete energy analysis which will be made in the following subsections.

From this definition, the $\mathbf{v}_b$ vectors can be calculated as

$$\mathbf{v}_{b,i-1/2,i-1} := \left[\frac{\partial e_{b,i-1/2}}{\partial \mathbf{q}_{i-1}} \right]^T = \begin{bmatrix} -\frac{1}{4} \frac{q_{3,i-1/2}^2}{\bar{q}_{1,i-1/2}^2} + \frac{1}{2} g_n \left(\frac{d\tilde{H}_U}{dA_U} \right)_{i-1} \\ -\frac{1}{4} \frac{q_{4,i-1/2}^2}{\bar{q}_{2,i-1/2}^2} + \frac{1}{2} g_n \left(\frac{d\tilde{H}_L}{dA_L} \right)_{i-1} \\ 0 \\ 0 \end{bmatrix},$$

$$\mathbf{v}_{b,i-1/2,i} := \left[\frac{\partial e_{b,i-1/2}}{\partial \mathbf{q}_i} \right]^T = \begin{bmatrix} -\frac{1}{4} \frac{q_{3,i-1/2}^2}{\bar{q}_{1,i-1/2}^2} + \frac{1}{2} g_n \left(\frac{d\tilde{H}_U}{dA_U} \right)_i \\ -\frac{1}{4} \frac{q_{4,i-1/2}^2}{\bar{q}_{2,i-1/2}^2} + \frac{1}{2} g_n \left(\frac{d\tilde{H}_L}{dA_L} \right)_i \\ \frac{q_{3,i-1/2}}{\bar{q}_{1,i-1/2}} \\ \frac{q_{4,i-1/2}}{\bar{q}_{2,i-1/2}} \end{bmatrix}.$$

The sum of the dot products of $\mathbf{v}_{b,i-1/2,i-1}$ and $\mathbf{v}_{b,i-1/2,i}$ with Eq. (36) for $\mathbf{q}_{i-1}$ and $\mathbf{q}_i$ respectively is

$$\left\langle \mathbf{v}_{b,i-1/2,i-1}, \frac{d\mathbf{q}_{i-1}}{dt} \right\rangle + \left\langle \mathbf{v}_{b,i-1/2,i}, \frac{d\mathbf{q}_i}{dt} \right\rangle$$
$$+ \left\langle \mathbf{v}_{b,i-1/2,i-1}, [\![\mathbf{f}_{i-1}]\!] \right\rangle + \left\langle \mathbf{v}_{b,i-1/2,i}, [\![\mathbf{f}_i]\!] \right\rangle$$
$$+ \left\langle \mathbf{v}_{b,i-1/2,i-1} \cdot \mathbf{j}_{i-1} \right\rangle [\![p_{i-3/2}]\!] + \left\langle \mathbf{v}_{b,i-1/2,i} \cdot \mathbf{j}_i \right\rangle [\![p_{i-1/2}]\!] = 0. \tag{40}$$

Using the following definitions:

$$\bar{\mathbf{v}}_{b,i,i-1/2} = \frac{1}{2} \left(\mathbf{v}_{b,i-1/2,i-1} + \mathbf{v}_{b,i+1/2,i} \right),$$

$$\bar{\mathbf{v}}_{b,i,i+1/2} = \frac{1}{2} \left(\mathbf{v}_{b,i-1/2,i} + \mathbf{v}_{b,i+1/2,i+1} \right),$$

$$[\![\mathbf{v}_{b,i,i-1/2}]\!] = \mathbf{v}_{b,i+1/2,i} - \mathbf{v}_{b,i-1/2,i-1},$$

$$[\![\mathbf{v}_{b,i,i+1/2}]\!] = \mathbf{v}_{b,i+1/2,i+1} - \mathbf{v}_{b,i-1/2,i},$$

and in addition discrete versions of the geometric relations (A.6),[1] the volumetric flow constraint (38), and substituting our discretization given by (37), it can be shown that the terms in (40) can be written in conservative form (Buist et al., 2022):

$$\left\langle \mathbf{v}_{b,i-1/2,i-1}, \frac{d\mathbf{q}_{i-1}}{dt} \right\rangle + \left\langle \mathbf{v}_{b,i-1/2,i}, \frac{d\mathbf{q}_i}{dt} \right\rangle = \frac{de_{b,i-1/2}}{dt},$$

---

[1] These are only exactly satisfied by geometries with $d^2 H_L / dA_L^2 = 0$ (for example the 2D channel geometry).
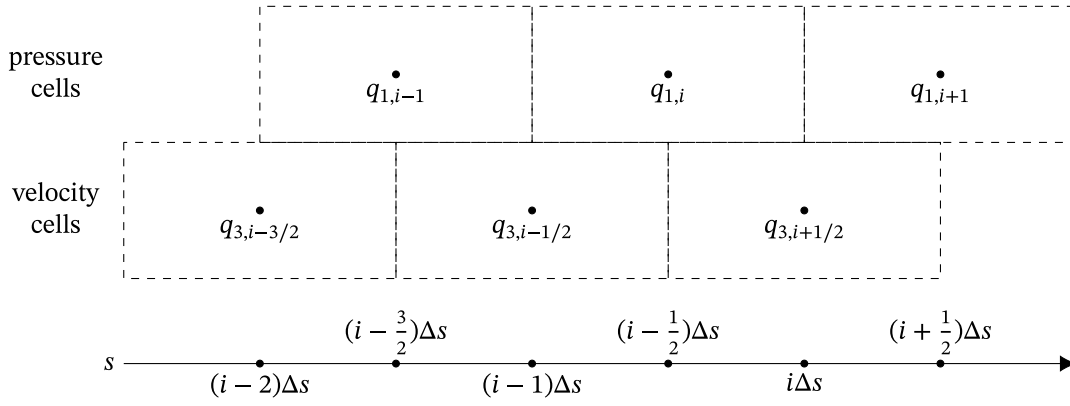
Fig. 2. Staggered grid layout.

$\left\langle \mathbf{v}_{b,i-1/2,i-1}, [\![\mathbf{f}_{i-1}]\!]\right\rangle + \left\langle \mathbf{v}_{b,i-1/2,i}, [\![\mathbf{f}_i]\!]\right\rangle = [\![h_{f,i-1/2}]\!],$

$\left\langle \mathbf{v}_{b,i-1/2,i-1}, \mathbf{j}_{i-1}\right\rangle [\![p_{i-3/2}]\!] + \left\langle \mathbf{v}_{b,i-1/2,i}, \mathbf{j}_i\right\rangle [\![p_{i-1/2}]\!] = [\![h_{p,i-1/2}]\!],$

with $h_{f,i}$ a discrete version of (6)[2]:

$$h_{f,i} = g_n \left(\frac{\mathrm{d}\widetilde{H}_U}{\mathrm{d}A_U}\right)_i \frac{\overline{q}_{3,i}}{\Delta s} + g_n \left(\frac{\mathrm{d}\widetilde{H}_L}{\mathrm{d}A_L}\right)_i \frac{\overline{q}_{4,i}}{\Delta s} + \left(\overline{\left[\left(\frac{q_{3,i}}{\overline{q}_{1,i}}\right)\right]^2} - \frac{1}{2}\overline{\left(\frac{q_{3,i}^2}{\overline{q}_{1,i}^2}\right)}\right)$$

$$\times \frac{\overline{q}_{3,i}}{\Delta s} + \left(\overline{\left[\left(\frac{q_{4,i}}{\overline{q}_{2,i}}\right)\right]^2} - \frac{1}{2}\overline{\left(\frac{q_{4,i}^2}{\overline{q}_{2,i}^2}\right)}\right)\frac{\overline{q}_{4,i}}{\Delta s}, \qquad (41)$$

and $h_{p,i}$ a discrete version of (7):

$$h_{p,i} = Q(t)p_i. \qquad (42)$$

The energy analysis of the additional model terms, given in Section 3.4 onward, will be fit into the same structure. The sum of the dot products of $\mathbf{v}_{b,i-1/2,i-1}$ and $\mathbf{v}_{b,i-1/2,i}$ with the additional model term will yield the resulting addition to the energy equation.

Since each term in (40) can be written in conservative form, it reduces to the local energy conservation equation

$$\frac{\mathrm{d}e_{b,i-1/2}}{\mathrm{d}t} + [\![h_{b,i-1/2}]\!] = 0, \qquad (43)$$

with $h_{b,i} = h_{f,i} + h_{p,i}$. Like in the continuous case, this equation can be integrated over a closed or periodic domain to yield

$$\frac{\mathrm{d}\widehat{E}_b}{\mathrm{d}t} = 0, \quad \text{with} \quad \widehat{E}_b(t) = \sum_{i=1}^{N_u} e_{b,i-1/2}(t),$$

which means that the discrete mechanical energy defined by (39) is a secondary conserved quantity of the semi-discrete model described in Section 3.1.

3.3. Energy equation for the semi-discrete extended model

Having introduced the energy-conserving discretization of the basic TFM and its energy conservation equation, we will propose discretizations of the three additions to the basic model, that retain the energy properties of their continuous counterparts, which were derived in Section 2. We will present discretizations of friction and diffusion that are strictly dissipative, and a discretization of surface tension that conserves the discretized energy, extended with a discrete version of the surface energy.

Additionally, we will present an upwind discretization of the advective terms that can be shown to be strictly dissipative, in contrast

to the energy-conserving discretization of the advective terms given by (37a). We will then propose to combine this upwind advective flux with the energy-conserving advective flux (using flux limiters), to produce a combined flux that is strictly dissipative, but less dissipative and less diffusive than the purely upwind flux. The combined flux is energy stable, and adds numerical dissipation only where necessary: near strong gradients and discontinuities. This mimics the behavior of weak solutions to the (basic) continuous equations, which instead of the energy equality of Section 2.2 (that is only valid for smooth solutions), will satisfy an energy inequality.

The semi-discrete model, extended with all the additional terms, is given by

$$\boxed{\frac{\mathrm{d}\mathbf{q}_i}{\mathrm{d}t} + [\![\mathbf{f}_i]\!] + \mathbf{j}_i [\![p_{i-1/2}]\!] = [\![\mathbf{d}_i]\!] + \mathbf{s}_i \Delta s + \mathbf{c}_{g,i}\Delta s + \mathbf{c}_{f,i}\Delta s + \mathbf{c}_{p,i}\Delta s} \qquad (44)$$

with $[\![\mathbf{d}_i]\!]$ representing diffusion, $\mathbf{c}_{f,i}$ representing friction, and $\mathbf{s}_i$ representing surface tension. The expressions for these terms will be given in (50), (54), and (56), respectively. The extended semi-discrete model includes the following contributions from streamwise gravity:

$$\mathbf{c}_{g,i}^T = \begin{bmatrix} 0 & 0 & -g\frac{[\![y_{i-1/2}]\!]}{\Delta s}\frac{\overline{q}_{1,i-1/2}}{\Delta s} & -g\frac{[\![y_{i-1/2}]\!]}{\Delta s}\frac{\overline{q}_{2,i-1/2}}{\Delta s} \end{bmatrix} \quad \text{with}$$

$$\frac{[\![y_{i-1/2}]\!]}{\Delta s} = [\sin(\phi)]_{i-1/2},$$

and from a constant driving pressure gradient:

$$\mathbf{c}_{p,i}^T = \begin{bmatrix} 0 & 0 & -\frac{\overline{q}_{1,i-1/2}}{\rho_U \Delta s}\frac{\partial p_{\text{body}}}{\partial s} & -\frac{\overline{q}_{2,i-1/2}}{\rho_L \Delta s}\frac{\partial p_{\text{body}}}{\partial s} \end{bmatrix}.$$

The energy equation that follows from (44) reads

$$\boxed{\frac{\mathrm{d}e_{i-1/2}}{\mathrm{d}t} + [\![h_{i-1/2}]\!] + [\![h_{n,i-1/2}]\!] = -\epsilon_{i-1/2} - \epsilon_{n,i-1/2} + c_{p,i-1/2}} \qquad (45)$$

with

$$e_{i-1/2} = e_{b,i-1/2} + e_{g,i-1/2} + e_{\sigma,i-1/2}, \qquad (46)$$

$$h_i = h_{b,i} + h_{g,i} + h_{d,i} + h_{\sigma,i}, \qquad (47)$$

$$\epsilon_{i-1/2} = \epsilon_{d,i-1/2} + \epsilon_{f,i-1/2}. \qquad (48)$$

The upcoming subsections will give the expressions (52) for $h_{d,i}$, (53) for $\epsilon_{d,i-1/2}$, (55) for $\epsilon_{f,i-1/2}$, (59) for $e_{\sigma,i-1/2}$, and (60) for $h_{\sigma,i}$. The contributions from streamwise gravity are given by (Buist et al., 2023)[3]

$$e_{g,i-1/2} = \overline{g\left(y_{i-1/2}\left(q_{1,i-1/2} + q_{2,i-1/2}\right)\right)}, \quad h_{g,i} = \overline{gy_i\left(\frac{q_{3,i}}{\Delta s} + \frac{q_{4,i}}{\Delta s}\right)},$$

and the contribution of the driving pressure gradient is given by

$$c_{p,i-1/2} = -Q_{i-1/2}\frac{\partial p_{\text{body}}}{\partial s}\Delta s,$$

---

[2] The given expression for $h_{f,i}$ is different from, but equivalent to, the expression given in Buist et al. (2023) (under the current assumptions).

[3] The given expression for $h_{g,i}$ is different from, but equivalent to, the expression given in Buist et al. (2023).

which is positive when the body force is aligned with the mean flow. These are all semi-discrete counterparts of the continuous expressions given in Section 2. The terms with subscript n are specific to the semi-discrete setting, and stem from the energy-stable combined advective flux. The numerical energy flux $h_{n,i}$ will be given by (65) and the numerical dissipation $\epsilon_{n,i-1/2}$ will be given by (66).

Eq. (45) is the second main novel result of this work, as it shows that we have obtained a semi-discrete model with the same energy conservation properties as the continuous model. The model additions that were conservative in the continuous setting are discretized in such a way that the energy-conserving behavior is retained, and the model additions that were dissipative in the continuous setting are discretized in such a way that the strictly dissipative behavior is retained. The local energy equation (45) can be integrated over a periodic domain to yield the global energy equation

$$\boxed{\frac{\mathrm{d}\widehat{E}}{\mathrm{d}t} = -\widehat{\mathcal{E}} - \widehat{\mathcal{E}}_n + \widehat{C}_p} \quad \text{with} \tag{49a}$$

$$\widehat{E}(t) = \sum_{i=1}^{N_u} e_{i-1/2}(t), \quad \widehat{\mathcal{E}} = \sum_{i=1}^{N_u} \epsilon_{i-1/2}(t), \quad \widehat{\mathcal{E}}_n = \sum_{i=1}^{N_u} \epsilon_{n,i-1/2}(t), \tag{49b}$$

$$\widehat{C}_p = \sum_{i=1}^{N_u} c_{p,i-1/2}(t) = -Q(t)\frac{\partial p_{\text{body}}}{\partial s}L. \tag{49c}$$

This equation determines that the energy of the solution can never increase, except due to an explicitly applied external force (through the source term $\widehat{C}_p$).

Therefore, the novel semi-discrete model is energy stable. It has physical and numerical dissipation rates ($\widehat{\mathcal{E}}$ and $\widehat{\mathcal{E}}_n$) that can be computed from the solution. These dissipation rates can be integrated in time numerically to find the total dissipated energy due to the different contributions. The total dissipated energy between two points in time should match the difference in energy between these two points in time, as calculated through an evaluation of $\widehat{E}$ at those two points in time.

Each term in the semi-discrete model independently results in corresponding terms in the energy equation. The combined result for the complete extended model, discretized in an energy-consistent manner, was given here. In the following subsections we will detail the novel contributions separately.

3.4. Physical diffusion

Our first novel contribution in the semi-discrete setting is to propose a discretization of the viscous diffusion terms and prove that it is strictly dissipative, just like its continuous counterpart. The diffusion term that can be added to the RHS of (36) is $\left[\partial\mathbf{d}/\partial s\right]_i \Delta s$, in which $\left[\partial\mathbf{d}/\partial s\right]_i$ is the discrete version of $\partial\mathbf{d}/\partial s$, with $\mathbf{d}$ given by (16). We propose the following straightforward central discretization, which yields the diffusion term in (44):

$$\left[\frac{\partial\mathbf{d}}{\partial s}\right]_i = \frac{1}{\Delta s}[\![\mathbf{d}_i]\!] = \frac{1}{\Delta s}\left(\mathbf{d}_{i+1/2} - \mathbf{d}_{i-1/2}\right),$$

with

$$\mathbf{d}_{i-1/2} := \begin{bmatrix} d_{1,i-1/2} \\ d_{2,i-1/2} \\ d_{3,i-1} \\ d_{4,i-1} \end{bmatrix} = \begin{bmatrix} 0 \\ 0 \\ \nu_{\text{eff},U}\frac{q_{1,i-1}}{(\Delta s)^2}\left[\!\left[\frac{q_{3,i-1}}{\overline{q}_{1,i-1}}\right]\!\right] \\ \nu_{\text{eff},L}\frac{q_{2,i-1}}{(\Delta s)^2}\left[\!\left[\frac{q_{4,i-1}}{\overline{q}_{2,i-1}}\right]\!\right] \end{bmatrix} = \begin{bmatrix} 0 \\ 0 \\ \rho_U\nu_{\text{eff},U}A_{U,i-1}\frac{[\![u_{U,i-1}]\!]}{\Delta s} \\ \rho_L\nu_{\text{eff},L}A_{L,i-1}\frac{[\![u_{L,i-1}]\!]}{\Delta s} \end{bmatrix}. \tag{50}$$

With diffusion, no extra term is added to the energy. The steps of the derivation of Section 3.2 can be simply repeated. With the proposed

discretization, the only additional terms in the energy equation (on the LHS) are

$$-\left\langle\mathbf{v}_{b,i-1/2,i-1},[\![\mathbf{d}_{i-1}]\!]\right\rangle - \left\langle\mathbf{v}_{b,i-1/2,i},[\![\mathbf{d}_i]\!]\right\rangle$$

$$= -[\![\left\langle\overline{\mathbf{v}}_{b,i-1/2,i-1},\mathbf{d}_{i-1}\right\rangle]\!] - [\![\left\langle\overline{\mathbf{v}}_{b,i-1/2,i},\mathbf{d}_i\right\rangle]\!]$$

$$\quad + \overline{\left\langle[\![\mathbf{v}_{b,i-1/2,i-1}]\!],\mathbf{d}_{i-1}\right\rangle} + \overline{\left\langle[\![\mathbf{v}_{b,i-1/2,i}]\!],\mathbf{d}_i\right\rangle}$$

$$= -\left[\!\!\left[\nu_{\text{eff},U}\frac{q_{1,i-1/2}}{(\Delta s)^2}\left(\frac{q_{3,i-1/2}}{\overline{q}_{1,i-1/2}}\right)\left[\!\left[\frac{q_{3,i-1/2}}{\overline{q}_{1,i-1/2}}\right]\!\right]\right]\!\!\right]$$

$$\quad + \overline{\left(\nu_{\text{eff},U}\frac{q_{1,i-1/2}}{(\Delta s)^2}\left[\!\left[\frac{q_{3,i-1/2}}{\overline{q}_{1,i-1/2}}\right]\!\right]^2\right)}$$

$$\quad - \left[\!\!\left[\nu_{\text{eff},L}\frac{q_{2,i-1/2}}{(\Delta s)^2}\left(\frac{q_{4,i-1/2}}{\overline{q}_{2,i-1/2}}\right)\left[\!\left[\frac{q_{4,i-1/2}}{\overline{q}_{2,i-1/2}}\right]\!\right]\right]\!\!\right]$$

$$\quad + \overline{\left(\nu_{\text{eff},L}\frac{q_{2,i-1/2}}{(\Delta s)^2}\left[\!\left[\frac{q_{4,i-1/2}}{\overline{q}_{2,i-1/2}}\right]\!\right]^2\right)}$$

$$= [\![h_{d,i-1/2}]\!] + \epsilon_{d,i-1/2}, \tag{51}$$

with

$$h_{d,i} = -\nu_{\text{eff},U}\frac{q_{1,i}}{(\Delta s)^2}\frac{1}{2}\left[\!\!\left[\left(\frac{q_{3,i}}{\overline{q}_{1,i}}\right)^2\right]\!\!\right] - \nu_{\text{eff},L}\frac{q_{2,i}}{(\Delta s)^2}\frac{1}{2}\left[\!\!\left[\left(\frac{q_{4,i}}{\overline{q}_{2,i}}\right)^2\right]\!\!\right], \tag{52}$$

$$\epsilon_{d,i-1/2} = \overline{\left(\nu_{\text{eff},U}\frac{q_{1,i-1/2}}{(\Delta s)^2}\left[\!\left[\frac{q_{3,i-1/2}}{\overline{q}_{1,i-1/2}}\right]\!\right]^2\right)} + \overline{\left(\nu_{\text{eff},L}\frac{q_{2,i-1/2}}{(\Delta s)^2}\left[\!\left[\frac{q_{4,i-1/2}}{\overline{q}_{2,i-1/2}}\right]\!\right]^2\right)}. \tag{53}$$

Here we have used a discrete product rule:

$$a_i[\![b_i]\!] = [\![\overline{a}_i b_i]\!] - \overline{([\![a_i]\!]b_i)},$$

and a discrete chain rule:

$$\overline{a}_{i-1/2}[\![a_{i-1/2}]\!] = \frac{1}{2}\left[\!\left[a_{i-1/2}^2\right]\!\right].$$

These can be derived by substituting the definitions (33) and (34), and applying some algebraic manipulation.

The result of (51) compares directly to the continuous result, given by (17). Like the continuous result, it consists of a conservative part, and a strictly dissipative part. The latter is due to $\epsilon_{d,i-1/2}$ being strictly positive, and the minus sign that is added when $\epsilon_{d,i-1/2}$ is moved to the RHS. Therefore, it has been proven that the proposed discretization of the diffusion terms is strictly dissipative with respect to the energy given by (46). Moreover, an explicit expression for the dissipation rate has been obtained, that can be used to measure the dissipation taking place in a numerical simulation.

3.5. Friction terms

Our second novel contribution in the semi-discrete setting is to show that wall and interface friction result in a strictly dissipative contribution to the semi-discrete energy equation. In (44), friction is included through the term $\mathbf{c}_{f,i}\Delta s$, in which $\mathbf{c}_{f,i}$ is the discrete version of (20). With reference to the closure relations given in Section 2.5, we assume the following functional dependencies for the discrete friction terms:

$$\tau_{L,i-1/2} := \tau_L(f_{L,i-1/2}, u_{L,i-1/2}), \quad \tau_{U,i-1/2} := \tau_U(f_{U,i-1/2}, u_{U,i-1/2}),$$

$$\tau_{\text{int},i-1/2} := \tau_{\text{int}}(f_{\text{int},i-1/2}, u_{U,i-1/2}, u_{L,i-1/2}),$$

with primitive variables given by (35). Then we propose the following discretization of the friction source terms:

$$\mathbf{c}_{f,i} = \begin{bmatrix} c_{f,1,i} \\ c_{f,2,i} \\ c_{f,3,i-1/2} \\ c_{f,4,i-1/2} \end{bmatrix} = \begin{bmatrix} 0 \\ 0 \\ \tau_{U,i-1/2}P_{U,i-1/2} + \tau_{\text{int},i-1/2}P_{\text{int},i-1/2} \\ \tau_{L,i-1/2}P_{L,i-1/2} - \tau_{\text{int},i-1/2}P_{\text{int},i-1/2} \end{bmatrix}. \tag{54}$$

Like with diffusion, adding friction terms to the system does not change the energy definition. Since the friction terms do not involve derivatives, the derivation of the contribution to the energy equation is almost the same as in the continuous case. The only modification to the energy equation is that the following terms are added to the RHS:

$$\langle \mathbf{v}_{b,i-1/2,i-1}, \mathbf{c}_{f,i-1}\Delta s\rangle + \langle \mathbf{v}_{b,i-1/2,i}, \mathbf{c}_{f,i}\Delta s\rangle$$
$$= \frac{q_{3,i-1/2}}{\overline{q}_{1,i-1/2}}\left(\tau_{U,i-1/2}P_{U,i-1/2} + \tau_{\text{int},i-1/2}P_{\text{int},i-1/2}\right)\Delta s$$
$$+ \frac{q_{4,i-1/2}}{\overline{q}_{2,i-1/2}}\left(\tau_{L,i-1/2}P_{L,i-1/2} - \tau_{\text{int},i-1/2}P_{\text{int},i-1/2}\right)\Delta s$$
$$= -\epsilon_{f,i-1/2},$$

with

$$\epsilon_{f,i-1/2} = \frac{1}{2}f_{U,i-1/2}\rho_U\left(\frac{q_{3,i-1/2}}{\overline{q}_{1,i-1/2}}\right)^2\left|\frac{q_{3,i-1/2}}{\overline{q}_{1,i-1/2}}\right|P_{U,i-1/2}\Delta s$$
$$+ \frac{1}{2}f_{L,i-1/2}\rho_L\left(\frac{q_{4,i-1/2}}{\overline{q}_{2,i-1/2}}\right)^2\left|\frac{q_{4,i-1/2}}{\overline{q}_{2,i-1/2}}\right|P_{L,i-1/2}\Delta s$$
$$+ \frac{1}{2}f_{\text{int},i-1/2}\rho_U\left(\frac{q_{3,i-1/2}}{\overline{q}_{1,i-1/2}} - \frac{q_{4,i-1/2}}{\overline{q}_{2,i-1/2}}\right)^2\left|\frac{q_{3,i-1/2}}{\overline{q}_{1,i-1/2}} - \frac{q_{4,i-1/2}}{\overline{q}_{2,i-1/2}}\right|$$
$$\times P_{\text{int},i-1/2}\Delta s. \tag{55}$$

Since $f_{U,i-1/2}$, $f_{L,i-1/2}$, $f_{\text{int},i-1/2}$, ρ_U, ρ_L, $P_{U,i-1/2}$, $P_{L,i-1/2}$, and $P_{\text{int},i-1/2}$ must be positive, and the rest of the terms are either quadratic or absolute, $\epsilon_{f,i-1/2}$ must always be positive. Therefore, $-\epsilon_{f,i-1/2}$ will act as a sink in the energy equation.

This result allows us, for the first time, to compare the dissipation due to wall and interface friction with the dissipation due to axial diffusion. Both components of the dissipation rate can be computed from the numerical solution, integrated numerically over time, and compared to one another to determine which has dissipated the most energy.

3.6. Surface tension

Our third novel contribution in the semi-discrete setting is to propose a discretization of the surface tension, and show that it is energy-conserving. This is key in maintaining the energy-stable nature of the semi-discrete model, while contributing favorably to the linear stability properties of the model; see Section 4.

Surface tension is included in (44) through the term $\mathbf{s}_i\Delta s$, in which $\mathbf{s}_i$ is the discrete version of (25). A general form of the surface tension, analogous to (25), is given by

$$\mathbf{s}_i = \begin{bmatrix} 0 \\ 0 \\ 0 \\ \frac{\overline{q}_{2,i-1/2}}{\rho_L\Delta s}\frac{1}{\Delta s}[\![\Delta p]\!]_{i-1/2} \end{bmatrix}. \tag{56}$$

We restrict the analysis to the channel geometry, for which clear results were obtained in the continuous analysis, and propose the following discretization of the pressure jump given by (31b):

$$[\![\Delta p_{\text{int}}]\!]_i = \frac{\sigma}{\Delta s}\left[\!\!\left[\frac{[\![H_{L,i}]\!]}{\Delta s}\right]\!\!\right]. \tag{57}$$

This constitutes a straightforward discretization of the conventional approximation of the surface tension in the TFM.

With the proposed discretization, the extra terms on the LHS of the energy equation can be written as

$$-\langle \mathbf{v}_{b,i-1/2,i-1}, \mathbf{s}_{i-1}\Delta s\rangle - \langle \mathbf{v}_{b,i-1/2,i}, \mathbf{s}_i\Delta s\rangle$$
$$= -\frac{q_{4,i-1/2}}{\rho_L\Delta s}\left[\!\!\left[\frac{\sigma}{\Delta s}\left[\!\!\left[\frac{[\![H_{L,i-1/2}]\!]}{\Delta s}\right]\!\!\right]\right]\!\!\right]$$
$$= -\frac{\sigma}{\rho_L}\overline{\left[\!\!\left[\left(\frac{q_{4,i-1/2}}{\Delta s}\right)\frac{1}{\Delta s}\left[\!\!\left[\frac{[\![H_{L,i-1/2}]\!]}{\Delta s}\right]\!\!\right]\right]\!\!\right]}$$
$$+ \frac{\sigma}{\rho_L}\left(\left[\!\!\left[\frac{q_{4,i-1/2}}{\Delta s}\right]\!\!\right]\frac{1}{\Delta s}\overline{\left[\!\!\left[\frac{[\![H_{L,i-1/2}]\!]}{\Delta s}\right]\!\!\right]}\right)$$
$$= [\![h_{\sigma,i-1/2}]\!] + \frac{\sigma}{\rho_L}\left[\!\!\left[\frac{1}{\Delta s}\frac{dq_{2,i-1/2}}{dt}\right]\!\!\right]\overline{\frac{[\![H_{L,i-1/2}]\!]}{\Delta s}}$$
$$= [\![h_{\sigma,i-1/2}]\!] + \sigma\frac{d}{dt}\left(\frac{[\![H_{L,i-1/2}]\!]}{\Delta s}\right)[\![H_{L,i-1/2}]\!]$$
$$= [\![h_{\sigma,i-1/2}]\!] + \sigma\frac{de_{\sigma,i-1/2}}{dt}, \tag{58}$$

in which, based on (31), we have chosen to define the surface energy as:

$$e_{\sigma,i-1/2} = \sigma\Delta s\left(1 + \frac{1}{2}\left(\frac{[\![H_{L,i-1/2}]\!]}{\Delta s}\right)^2\right), \tag{59}$$

with an energy flux of

$$h_{\sigma,i} = \sigma\frac{1}{\Delta s}\left[\!\!\left[\frac{q_{4,i}}{\rho_L\Delta s}\right]\!\!\right]\overline{\left(\frac{[\![H_{L,i}]\!]}{\Delta s}\right)} - \sigma\overline{\left(\frac{q_{4,i}}{\rho_L\Delta s}\right)}\frac{1}{\Delta s}\left[\!\!\left[\frac{[\![H_{L,i}]\!]}{\Delta s}\right]\!\!\right]. \tag{60}$$

In this derivation, we have used a discrete version of the product rule that can be derived from (33) and (34):

$$\overline{[\![\overline{a}_{i-1/2}b_{i-1/2}]\!]} = \overline{\left([\![a_{i-1/2}]\!]\,\overline{b}_{i-1/2}\right)} + \overline{a}_{i-1/2}[\![b_{i-1/2}]\!],$$

and substituted the semi-discrete mass conservation equation for the lower fluid (the second equation of (36)), specified to the 2D channel.

The derivation (58) shows that, for the surface tension discretization given by (56) and (57), the contribution of surface tension to the semi-discrete energy equation can be written in conservative form. This requires adding an extra term to the energy, which must take a specific form that is tied to this discretization. We have succeeded in finding a combination of $[\![\Delta p_{\text{int}}]\!]_i$ and $e_{\sigma,i-1/2}$ that is energy-conserving. These results hold for the 2D channel geometry.

Therefore, we have found a way to add surface tension to the semi-discrete model, in such a way that it remains energy stable. Consistent with the physics of the flow, no dissipation (or production) of energy will result from surface tension. All dissipation can be attributed to effects that would physically be expected to yield dissipation: diffusion and wall and interface friction.

3.7. Numerical diffusion

In addition to the energy-consistent discretizations of the extra terms in the continuous model, a modification is needed to our discretization of the basic model, as given by (37). In this subsection we will propose an upwind discretization of the advective terms in the momentum equations, that can be shown to add a strictly dissipative term to the energy equation, and is therefore energy stable.

This is required because our energy-conserving central advective flux, included in (37a), is sensitive to discontinuities. At discontinuities, the proofs of energy conservation for the continuous equations no longer hold, and the continuous equations should dissipate energy (Jameson, 2008). However, our energy-conserving flux expressly forbids this. As a result, when discontinuities appear in the solution, numerical oscillations are generated. Adding physical diffusion mitigates the problem, but it acts at small scales, and in order to incorporate its full effect, a high grid refinement is required.

Therefore, it is necessary to introduce some form of (strictly dissipative) numerical diffusion. The adjective 'numerical' indicates that it should be grid-dependent: it is primarily needed at coarse resolutions. Such diffusion can be provided by an upwind discretization of the advective flux.

Different upwind discretizations can be conceived, by taking different interpolations and by upwinding different parts of the numerical flux, see e.g. Issa and Kempf (2003), Krasnopolsky and Lukyanov (2018) and Liao et al. (2008). Here we present a new upwind discretization that is based on the conservative variables, and closely resembles the energy-conserving flux of (37a), with the exception that for the advecting velocities we use an upwind interpolation, instead of a central interpolation:

$$f_{3,a,i-1,u} = \left(\frac{q_3}{q_1}\right)_{\text{up},i-1} \frac{\overline{q}_{3,i-1}}{\Delta s} = \rho_U u_{U,\text{up},i-1} \overline{\left(A_{U,i-1} u_{U,i-1}\right)}, \tag{61a}$$

$$f_{4,a,i-1,u} = \left(\frac{q_4}{q_2}\right)_{\text{up},i-1} \frac{\overline{q}_{4,i-1}}{\Delta s} = \rho_L u_{L,\text{up},i-1} \overline{\left(A_{L,i-1} u_{L,i-1}\right)}, \tag{61b}$$

with

$$u_{U,\text{up},i-1} = \begin{cases} u_{U,i-3/2}, & \text{if } \overline{q}_{3,i-1} > 0 \\ u_{U,i-1/2}, & \text{otherwise} \end{cases}$$

$$u_{L,\text{up},i-1} = \begin{cases} u_{L,i-3/2}, & \text{if } \overline{q}_{4,i-1} > 0 \\ u_{L,i-1/2}, & \text{otherwise} \end{cases}$$

This upwind flux is atypical in its choice to have u_U and u_L as the upwinded variables instead of q_3 and q_4, and in its choice to base the upwind directions on q_3 and q_4 instead of u_U and u_L. These choices are needed to prove the strictly dissipative property.

We only apply an upwind discretization to the advective terms of the momentum equations, and not to those of the mass equations. The mass equations are left unchanged, since changing these would cause complications in three areas. First, changing the mass advective fluxes would interfere with the coupling between the mass and momentum equations. Second, the discrete form of the volumetric flow constraint would be altered, since it is derived through substitution of the mass equations in the volume constraint. Third, the discrete energy analysis of the streamwise gravity and surface tension terms could be invalidated or require significant modification, since it involves substitution of the mass equations.

We now show that the contribution to the energy equation of these upwind fluxes can be divided into a conservative part and a non-conservative part. To this end, the analysis of Section 3.2 is repeated, this time with (61) taking the place of the momentum advection part of the fluxes given in (37a). The contribution of the flux terms to (40) can then be written as

$$\langle \mathbf{v}_{b,i-1/2,i-1}, [\![\mathbf{f}_{i-1}]\!]\rangle + \langle \mathbf{v}_{b,i-1/2,i}, [\![\mathbf{f}_i]\!]\rangle$$
$$= [\![\langle \overline{\mathbf{v}}_{b,i-1/2,i-1}, \mathbf{f}_{i-1}\rangle]\!] + [\![\langle \overline{\mathbf{v}}_{b,i-1/2,i}, \mathbf{f}_i\rangle]\!]$$
$$\quad - \langle [\![\mathbf{v}_{b,i-1/2,i-1}]\!], \mathbf{f}_{i-1}\rangle - \langle [\![\mathbf{v}_{b,i-1/2,i}]\!], \mathbf{f}_i\rangle$$
$$= [\![h_{f,i-1/2}]\!] + [\![h_{u,i-1/2}]\!] + \epsilon_{u,i-1/2},$$

with $h_{f,i}$ given by (41), $h_{u,i}$ given by

$$h_{u,i} = -\overline{\left(\frac{q_{3,i}}{q_{1,i}}\right)}\left(\left(\frac{q_{3,i}}{q_{1,i}}\right) - \left(\frac{q_3}{q_1}\right)_{\text{up},i}\right)\frac{\overline{q}_{3,i}}{\Delta s}$$
$$\quad - \overline{\left(\frac{q_{4,i}}{q_{2,i}}\right)}\left(\left(\frac{q_{4,i}}{q_{2,i}}\right) - \left(\frac{q_4}{q_2}\right)_{\text{up},i}\right)\frac{\overline{q}_{4,i}}{\Delta s}, \tag{62}$$

and $\epsilon_{u,i-1/2}$ given by

$$\epsilon_{u,i-1/2} = \epsilon_{u,U,i-1/2} + \epsilon_{u,L,i-1/2}$$
$$= \left(\left[\!\!\left[\frac{q_{3,i-1/2}}{q_{1,i-1/2}}\right]\!\!\right]\left(\overline{\left(\frac{q_{3,i-1/2}}{q_{1,i-1/2}}\right)} - \left(\frac{q_3}{q_1}\right)_{\text{up},i-1/2}\right)\frac{\overline{q}_{3,i-1/2}}{\Delta s}\right.$$

$$\left. + \overline{\left[\!\!\left[\frac{q_{4,i-1/2}}{q_{2,i-1/2}}\right]\!\!\right]\left(\overline{\left(\frac{q_{4,i-1/2}}{q_{2,i-1/2}}\right)} - \left(\frac{q_4}{q_2}\right)_{\text{up},i-1/2}\right)\frac{\overline{q}_{4,i-1/2}}{\Delta s}}\right). \tag{63}$$

We have split $\epsilon_{u,i-1/2}$ into a part pertaining to the upper fluid ($\epsilon_{u,U,i-1/2}$, first line) and a part pertaining to the lower fluid ($\epsilon_{u,L,i-1/2}$, second line).

This shows that the contribution of the upwind flux can be written as the contribution $[\![h_{f,i-1/2}]\!]$ of the energy-conserving flux, plus some extra terms. Some of these terms are completely between double brackets, meaning they are energy-conserving, and can be included in the energy flux $h_{u,i}$. The remaining terms will become source terms in the energy equation.

We will now show that these source terms are strictly dissipative. It is sufficient to only examine the terms pertaining to the upper fluid, since the terms pertaining to the lower fluid have the same structure, so their analysis will yield similar results. The source terms for the upper fluid can be rewritten in the following manner:

$$\epsilon_{u,U,i-1/2} = \frac{1}{2}\left[\!\!\left[\frac{q_{3,i-1}}{q_{1,i-1}}\right]\!\!\right]\frac{\overline{q}_{3,i-1}}{\Delta s}\left[\overline{\left(\frac{q_{3,i-1}}{q_{1,i-1}}\right)} - \left(\frac{q_3}{q_1}\right)_{\text{up},i-1}\right]$$
$$\quad + \frac{1}{2}\left[\!\!\left[\frac{q_{3,i}}{q_{1,i}}\right]\!\!\right]\frac{\overline{q}_{3,i}}{\Delta s}\left[\overline{\left(\frac{q_{3,i}}{q_{1,i}}\right)} - \left(\frac{q_3}{q_1}\right)_{\text{up},i}\right].$$

Now, we consider the case that $\overline{q}_{3,i-1} > 0$ and $\overline{q}_{3,i} > 0$, so that $u_{U,\text{up},i-1} = u_{U,i-3/2}$ and $u_{U,\text{up},i} = u_{U,i-1/2}$:

$$\epsilon_{u,U,i-1/2} = \frac{1}{2}\left[\!\!\left[\frac{q_{3,i-1}}{q_{1,i-1}}\right]\!\!\right]\frac{\overline{q}_{3,i-1}}{\Delta s}\left[\overline{\left(\frac{q_{3,i-1}}{q_{1,i-1}}\right)} - \frac{q_{3,i-3/2}}{\overline{q}_{1,i-3/2}}\right]$$
$$\quad + \frac{1}{2}\left[\!\!\left[\frac{q_{3,i}}{q_{1,i}}\right]\!\!\right]\frac{\overline{q}_{3,i}}{\Delta s}\left[\overline{\left(\frac{q_{3,i}}{q_{1,i}}\right)} - \frac{q_{3,i-1/2}}{\overline{q}_{1,i-1/2}}\right]$$
$$= \frac{1}{4}\left[\!\!\left[\frac{q_{3,i-1}}{q_{1,i-1}}\right]\!\!\right]^2\frac{\overline{q}_{3,i-1}}{\Delta s} + \frac{1}{4}\left[\!\!\left[\frac{q_{3,i}}{q_{1,i}}\right]\!\!\right]^2\frac{\overline{q}_{3,i}}{\Delta s}.$$

Clearly, these terms must be positive, given that we have specified that $\overline{q}_{3,i-1} > 0$ and $\overline{q}_{3,i} > 0$.

Similarly, we consider the case that $\overline{q}_{3,i-1} < 0$ and $\overline{q}_{3,i} < 0$, so that $u_{U,\text{up},i-1} = u_{U,i-1/2}$ and $u_{U,\text{up},i} = u_{U,i+1/2}$:

$$\epsilon_{u,U,i-1/2} = \frac{1}{2}\left[\!\!\left[\frac{q_{3,i-1}}{q_{1,i-1}}\right]\!\!\right]\frac{\overline{q}_{3,i-1}}{\Delta s}\left[\overline{\left(\frac{q_{3,i-1}}{q_{1,i-1}}\right)} - \frac{q_{3,i-1/2}}{\overline{q}_{1,i-1/2}}\right]$$
$$\quad + \frac{1}{2}\left[\!\!\left[\frac{q_{3,i}}{q_{1,i}}\right]\!\!\right]\frac{\overline{q}_{3,i}}{\Delta s}\left[\overline{\left(\frac{q_{3,i}}{q_{1,i}}\right)} - \frac{q_{3,i+1/2}}{\overline{q}_{1,i+1/2}}\right]$$
$$= -\frac{1}{4}\left[\!\!\left[\frac{q_{3,i-1}}{q_{1,i-1}}\right]\!\!\right]^2\frac{\overline{q}_{3,i-1}}{\Delta s} - \frac{1}{4}\left[\!\!\left[\frac{q_{3,i}}{q_{1,i}}\right]\!\!\right]^2\frac{\overline{q}_{3,i}}{\Delta s}.$$

Again, these terms must be positive, given that we have specified that $\overline{q}_{3,i-1} < 0$ and $\overline{q}_{3,i} < 0$. The third and fourth options (with differing signs between $\overline{q}_{3,i-1}$ and $\overline{q}_{3,i}$) are just simple recombinations of these two results, so they too will be strictly positive. Move these terms to the RHS, and they become strictly negative source terms. This means that our proposed upwind discretization adds a strictly negative source term to the energy equation, which acts to dissipate the energy given by (46).

Comparing this numerical dissipation term to the physical dissipation term given by (53), we see that, among other differences, the numerical dissipation has an additional factor Δs. It is proportional to the cell size and will decrease at a first order rate with increasing grid resolution.

Note that alternative upwind fluxes, such as those used by Krasnopolsky and Lukyanov (2018) and Liao et al. (2008), do not yield contributions to the energy equation that can be written as the sum of a conservative term and a strictly negative dissipation term. In contrast, our new upwind advective numerical flux does possess the property of energy stability. However, it may be more dissipative than necessary, and for this reason we will combine it with the energy-conserving flux, in an energy-stable manner.

3.8. Energy-stable combined advective flux

Our fifth and key novel contribution in the semi-discrete setting is that we combine the strictly dissipative upwind advective flux with the energy-conserving central advective flux, in such a way that the resulting advective flux is energy stable, but less dissipative than a purely upwind discretization. The proposed combination possesses the best properties of both schemes.

Our energy-conserving advective fluxes were defined in (37a) as

$$f_{3,a,i-1,\text{ec}} = \overline{\left(\frac{q_{3,i-1}}{\overline{q}_{1,i-1}}\right)} \frac{\overline{q}_{3,i-1}}{\Delta s} = \rho_U \overline{u}_{U,i-1} \overline{\left(\overline{A}_{U,i-1} u_{U,i-1}\right)},$$

$$f_{4,a,i-1,\text{ec}} = \overline{\left(\frac{q_{4,i-1}}{\overline{q}_{2,i-1}}\right)} \frac{\overline{q}_{4,i-1}}{\Delta s} = \rho_L \overline{u}_{L,i-1} \overline{\left(\overline{A}_{L,i-1} u_{L,i-1}\right)}.$$

Following the conventional manner of combining low-order and higher-order fluxes (Toro, 1999), we propose the following combination of the energy-conserving fluxes and the upwind fluxes given by (61), using flux limiters:

$$f_{3,a,i-1} = \left(1 - \phi\left(r_{U,i-1}\right)\right) f_{3,a,i-1,u} + \phi\left(r_{U,i-1}\right) f_{3,a,i-1,\text{ec}}, \tag{64a}$$

$$f_{4,a,i-1} = \left(1 - \phi\left(r_{L,i-1}\right)\right) f_{4,a,i-1,u} + \phi\left(r_{L,i-1}\right) f_{4,a,i-1,\text{ec}}, \tag{64b}$$

with $\phi(r_{U,i-1})$ and $\phi(r_{L,i-1})$ the limiter functions which determine the weighting between the upwind flux and the energy-conserving flux. Here, the upwind flux is a low-order flux, and the energy-conserving flux is a higher-order flux. The limiting coefficients depend on the slope of the solution:

$$r_{U,i-1} = \begin{cases} \frac{q_{3,i-5/2} - q_{3,i-3/2}}{q_{3,i-3/2} - q_{3,i-1/2}}, & \text{if } \overline{u}_{U,i-1} > 0 \\ 1, & \text{if } \overline{u}_{U,i-1} = 0 \\ \frac{q_{3,i-1/2} - q_{3,i+1/2}}{q_{3,i-3/2} - q_{3,i-1/2}}, & \text{if } \overline{u}_{U,i-1} < 0 \end{cases}$$

$$r_{L,i-1} = \begin{cases} \frac{q_{4,i-5/2} - q_{4,i-3/2}}{q_{4,i-3/2} - q_{4,i-1/2}}, & \text{if } \overline{u}_{L,i-1} > 0 \\ 1, & \text{if } \overline{u}_{L,i-1} = 0 \\ \frac{q_{4,i-1/2} - q_{4,i+1/2}}{q_{4,i-3/2} - q_{4,i-1/2}}, & \text{if } \overline{u}_{L,i-1} < 0 \end{cases}$$

These coefficients are fed to the limiter functions, for which many options exist. Here we choose the minmod function:

$$\phi(r) = \max\left[0, \min\left(r, 1\right)\right].$$

The minmod function will always yield a value between 0 and 1, which is an important property that we need to show energy stability of the combined scheme. When the solution is smooth, $\phi(r)$ will be close to 1, and the energy-conserving flux will be used. When the solution is less smooth, the upwind flux will be weighted more heavily. We note that the minmod function could be exchanged for a less dissipative alternative, though most conventional limiter functions are disqualified due to the requirement that the limiter function yield a value between 0 and 1.

The energy analysis of Section 3.7 can be repeated for the fluxes given by (64), with similar results. The contribution of the flux terms to (40) can be written as

$$\left\langle \mathbf{v}_{b,i-1/2,i-1}, [\![\mathbf{f}_{i-1}]\!] \right\rangle + \left\langle \mathbf{v}_{b,i-1/2,i}, [\![\mathbf{f}_i]\!] \right\rangle$$
$$= [\![\left\langle \overline{\mathbf{v}}_{b,i-1/2,i-1}, \mathbf{f}_{i-1} \right\rangle]\!] + [\![\left\langle \overline{\mathbf{v}}_{b,i-1/2,i}, \mathbf{f}_i \right\rangle]\!]$$
$$\quad - \left\langle [\![\mathbf{v}_{b,i-1/2,i-1}]\!], \mathbf{f}_{i-1} \right\rangle - \left\langle [\![\mathbf{v}_{b,i-1/2,i}]\!], \mathbf{f}_i \right\rangle$$
$$= [\![h_{f,i-1/2}]\!] + [\![h_{n,i-1/2}]\!] + \epsilon_{n,i-1/2},$$

with $h_{f,i}$ given by (41), $h_{n,i}$ given by

$$h_{n,i} = -\left(1 - \phi\left(r_{U,i}\right)\right) \overline{\left(\frac{q_{3,i}}{\overline{q}_{1,i}}\right)} \left(\left(\frac{q_{3,i}}{\overline{q}_{1,i}}\right) - \left(\frac{q_3}{\overline{q}_1}\right)_{\text{up},i}\right) \frac{\overline{q}_{3,i}}{\Delta s}$$
$$\quad - \left(1 - \phi\left(r_{L,i}\right)\right) \overline{\left(\frac{q_{4,i}}{\overline{q}_{2,i}}\right)} \left(\left(\frac{q_{4,i}}{\overline{q}_{2,i}}\right) - \left(\frac{q_4}{\overline{q}_2}\right)_{\text{up},i}\right) \frac{\overline{q}_{4,i}}{\Delta s}, \tag{65}$$

and $\epsilon_{n,i-1/2}$ given by

$$\epsilon_{n,i-1/2}$$
$$= \overline{\left(\left(1 - \phi\left(r_{U,i-1/2}\right)\right) [\![\frac{q_{3,i-1/2}}{\overline{q}_{1,i-1/2}}]\!] \left(\left(\frac{q_{3,i-1/2}}{\overline{q}_{1,i-1/2}}\right) - \left(\frac{q_3}{\overline{q}_1}\right)_{\text{up},i-1/2}\right) \frac{\overline{q}_{3,i-1/2}}{\Delta s}\right)}$$
$$+ \overline{\left(\left(1 - \phi\left(r_{L,i-1/2}\right)\right) [\![\frac{q_{4,i-1/2}}{\overline{q}_{2,i-1/2}}]\!] \left(\left(\frac{q_{4,i-1/2}}{\overline{q}_{2,i-1/2}}\right) - \left(\frac{q_4}{\overline{q}_2}\right)_{\text{up},i-1/2}\right) \frac{\overline{q}_{4,i-1/2}}{\Delta s}\right)}. \tag{66}$$

Since with the minmod limiter function, the factors $\left(1 - \phi\left(r_{U,i}\right)\right)$ and $\left(1 - \phi\left(r_{L,i}\right)\right)$ have values between 0 and 1, this dissipation term has the same positivity property as the upwind dissipation term given by (63).

Therefore, our novel advective numerical flux, formed by combining our upwind flux and our energy-conserving flux, is energy stable. The new energy-stable flux will be less dissipative than the pure upwind flux, since it uses the energy-conserving flux where possible. Where the solution is smooth, the continuous equations conserve energy, and our energy-stable flux replicates this property. Where the solution is discontinuous, the energy-stable flux effectively adds numerical diffusion which dissipates energy.

4. Stability

In this section, we discuss the stability of the basic and extended TFM. The stability of the TFM is a topic that has received much attention since the discovery of the ill-posedness issue by Lyczkowski et al. (1978). Here we focus on providing a detailed motivation for our proposed model additions of physical diffusion and surface tension. Together these effects produce a reliable model that yields convergent solutions under flow conditions where the basic two-fluid model fails. Friction plays a less important role in the model's stability, but is an important physical effect that an accurate model must include, and is included in the stability analysis given here.

The basic two-fluid model, as described in Section 2.1, is known to be conditionally hyperbolic (Montini, 2011). In the region of state space where the velocity difference is below the inviscid Kelvin–Helmholtz (IKH) limit, the eigenvalues of the model are real, but outside this region the eigenvalues of the model are complex (Liao et al., 2008). Linear stability analysis (see Appendix C) confirms the issue put forward by the characteristic analysis: within the hyperbolic region the model is stable, but in the non-hyperbolic region the (linear) growth rates for small wavelength perturbations tend towards infinity. Therefore the model is said to be (linearly) ill-posed: the common view is that this precludes meaningful solutions to the continuous model, and prevents convergence of numerical solutions (Issa and Kempf, 2003). This prevents the use of the basic model in its non-hyperbolic region.

Fig. 3 is a stability map similar to those of Barnea and Taitel (1993, 1994). It maps the stability of steady states of the TFM, where friction is balanced by a constant driving pressure gradient (acting as a body force). The parameters are given in Table 1 and the geometry is that of a 2D channel. Given the lower fluid superficial velocity $u_L \alpha_L$ and the upper fluid superficial velocity $u_U(1 - \alpha_L)$, the hold-up $\alpha_L = A_L/A$ and driving pressure gradient $\partial p_{\text{body}}/\partial s$ follow from the demand for a fully developed steady state (derivatives to s and t must be zero). For these steady states, the two dispersion relations $\omega(\lambda)$ can be calculated according to Appendix C. For a given perturbation wavelength λ, we consider the dispersion relation for which the imaginary component of ω is largest: this is the most unstable mode for this wavelength. If for this most unstable mode $\text{Im}(\omega(\lambda)) < 0$, the steady state is stable and damping (to perturbations of wavelength λ), if $\text{Im}(\omega(\lambda)) = 0$ it is neutrally stable, and if $\text{Im}(\omega(\lambda)) > 0$ it is unstable. As long as $\text{Im}(\omega(\lambda))$ is bounded as $\lambda \to 0$, the state is well-posed. If $\text{Im}(\omega(\lambda)) \to \infty$ for $\lambda \to 0$, the state is labeled 'ill-posed'.
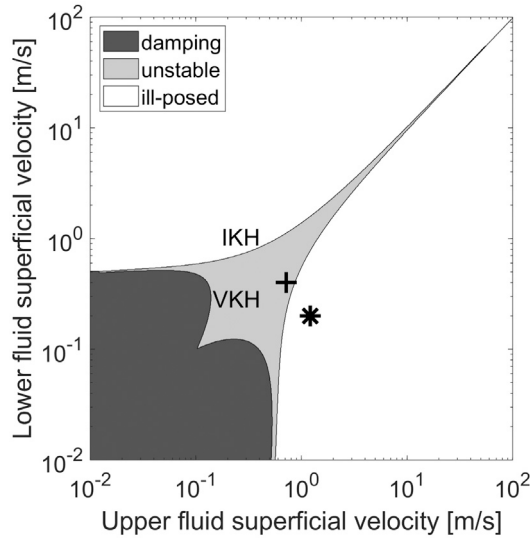
Fig. 3. A map of the linear stability of perturbations to steady states of the TFM with wall and interface friction, using the basic model without diffusion and surface tension. The state space is divided into regions where perturbations are damped, are unstable with a bounded growth rate, or are unstable with an unbounded growth rate (ill-posed). The inviscid Kelvin–Helmholtz (IKH) and viscous Kelvin–Helmholtz (VKH) stability boundaries are indicated. The symbol + marks the base state given by Table 2, and the symbol ∗ marks the base state given by Table 3.

Table 1
Parameters used for the linear stability analysis. These resemble the parameters of the Thorpe experiment (Thorpe, 1969) as described by Fullmer et al. (2014b).

Parameter	Symbol	Value	Units
Lower fluid density	ρ_L	1000	kg m^{-3}
Upper fluid density	ρ_U	780	kg m^{-3}
Acceleration of gravity	g	9.81	m s^{-2}
Channel inclination	ϕ	0	degrees
Channel height	H	0.03	m
Lower fluid material viscosity	$\nu_{m,L}$	$1.0 \cdot 10^{-6}$	$\text{m}^2 \text{s}^{-1}$
Upper fluid material viscosity	$\nu_{m,U}$	$1.9 \cdot 10^{-6}$	$\text{m}^2 \text{s}^{-1}$
Lower fluid effective viscosity	$\nu_{\text{eff},L}$	$1.13 \cdot 10^{-4}$	$\text{m}^2 \text{s}^{-1}$
Upper fluid effective viscosity	$\nu_{\text{eff},U}$	$1.21 \cdot 10^{-4}$	$\text{m}^2 \text{s}^{-1}$
Surface tension	σ	0.04	kg m s^{-2}

Table 2
Base state used for the linear stability analysis, corresponding to the left plot in Fig. 4, and marked with the symbol + in the stability maps.

Variable	Symbol	Value	Units
Initial lower fluid hold-up	$\alpha_{L,0}$	0.4	–
Initial lower fluid velocity	$u_{L,0}$	1	m s^{-1}
Initial upper fluid velocity	$u_{U,0}$	1.198	m s^{-1}
Driving pressure gradient	$\partial p_{\text{body}}/\partial s$	−204.2	$\text{kg m}^{-2} \text{s}^{-2}$

Table 3
Base state used for the linear stability analysis, corresponding to the right plot in Fig. 4, and marked with the symbol ∗ in the stability maps.

Variable	Symbol	Value	Units
Initial lower fluid hold-up	$\alpha_{L,0}$	0.2	–
Initial lower fluid velocity	$u_{L,0}$	1	m s^{-1}
Initial upper fluid velocity	$u_{U,0}$	1.515	m s^{-1}
Driving pressure gradient	$\partial p_{\text{body}}/\partial s$	−268.4	$\text{kg m}^{-2} \text{s}^{-2}$

For the basic model without diffusion and surface tension, stability is independent of wavelength (Jones and Prosperetti, 1985): if long wavelengths are unstable then short wavelengths are also unstable (though with different growth rates). This can be seen in Fig. 4 (similar to figure 3.2 in López de Bertodano et al. (2017)), which shows the growth rate of the most unstable mode, for two different steady states,

and for different versions of the TFM. Therefore the stability map of the basic model in Fig. 3 is independent of wavelength. It is divided into an ill-posed region and a well-posed region. Without friction the whole well-posed region would be neutrally stable. Friction divides the well-posed region of Fig. 3 into a region with damping and an unstable region (but with bounded growth rates). The stability boundary with friction is referred to as the viscous Kelvin–Helmholtz (VKH) boundary, while the ill-posedness boundary is referred to as the inviscid Kelvin–Helmholtz (IKH) boundary (Barnea and Taitel, 1993, 1994).

Adding physical diffusion and surface tension changes the dispersion relations, as can be seen in Fig. 4. Short wavelength perturbations are stabilized, while at long wavelengths, the dispersion relations are unchanged. The growth rate no longer tends to infinity for short wavelengths, removing the ill-posedness issue. In case only diffusion is added, the growth rate is bounded, but its value still increases rapidly at short wavelengths, which causes short wavelength perturbations to dominate the solution. In a numerical model, upon refining the grid, increasingly unstable scales are resolved, making it impossible to reach convergence (Holmås et al., 2008).

When both physical diffusion and surface tension are added to the model, as suggested by Fullmer et al. (2014b), a cut-off wavelength is introduced below which perturbations are damped, as can be seen in Fig. 4 at approximately $\lambda_c = 0.0174$ m. This removes the unphysical short wavelength instabilities. Meanwhile, the long wavelength instabilities, which are physical instabilities that are an integral part of the model, can still be resolved dynamically. The removal of the severe short wavelength instabilities means that the impediment to grid convergence is removed, and implies that theoretically all dynamics could be resolved without refining past $\Delta s = \lambda_c/2$. The combination of physical diffusion and surface tension is crucial to achieving the damping effect: with only surface tension the short wavelengths are nearly neutrally stable, with only the shortest wavelengths being very weakly damped, due to the influence of friction.

The cut-off wavelength depends on the state and model parameters. As the difference between the velocities of the two fluids is increased further into the region of instability beyond the IKH limit, the cut-off wavelength is decreased. This is apparent from comparing the stability maps for different wavelengths in Fig. 5. The marked states in the maps are unstable (with bounded growth rates) to long wavelength perturbations, but stable for short wavelengths, as shown in Fig. 4. For each possible state there will always be a cut-off wavelength below which damping takes place. Therefore, the extended model is unconditionally well-posed.

This method of regularization leaves intermediate scale perturbations intact that might lie outside of the range of validity of the model dictated by the long-wavelength assumption. An alternative option is to also damp these scales, by using artificial diffusion, added to both the mass and momentum equations (Bonzanini et al., 2017; Fullmer et al., 2014a; Holmås et al., 2008). However, the fact that these scales are not modeled to complete accuracy does not mean that it is more accurate to artificially eliminate these perturbations. Our approach is to leave these perturbations intact, for as far as they are not stabilized by physically motivated model components.

Depending on the state, the cut-off wavelength may become quite low and the instability quite severe. For such an unstable state, the solution will be dominated by intermediate scale instabilities, that lie above the cut-off wavelength, but are still of very short wavelength. Practically, the grid resolution required to reach the cut-off wavelength may be prohibitive. Therefore, in engineering applications, it may not be possible to resolve all the dynamics of the model in a numerical simulation. This does not affect the linear well-posedness: if the small scales are not resolved, they will cause no harm, and if they are resolved, they will be regularized by diffusion and surface tension.

The longer scale instabilities that remain present in our extended model have bounded growth rates, but would grow indefinitely, according to the linear stability analysis. In reality, when the perturbations
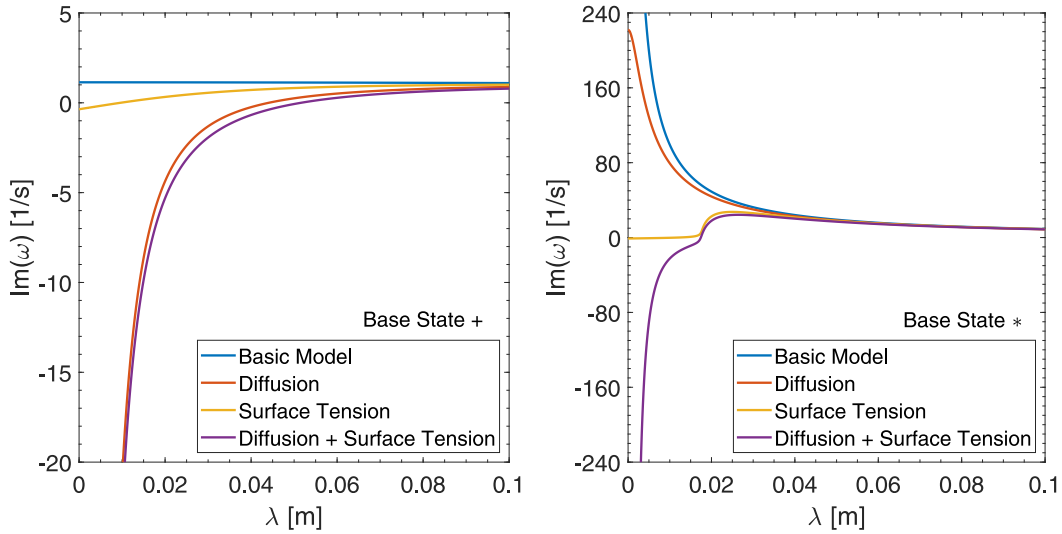
Fig. 4. Imaginary component of the angular frequency ω for the most unstable mode, for the set of parameters given in Table 1, plotted as a function of wavelength $\lambda = 2\pi/k$. All models include wall and interface friction. Left: base state given by Table 2, marked by the symbol + in the stability maps. Right: base state given by Table 3, marked by the symbol * in the stability maps.
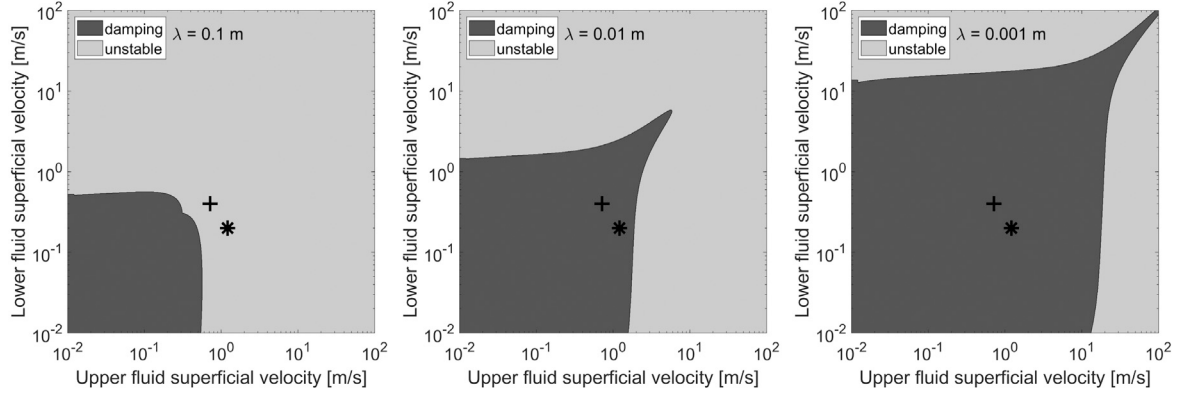

Fig. 5. Maps of the linear stability of short wavelength perturbations to steady states of the TFM, with wall and interface friction, diffusion, and surface tension. The stability of perturbations with a specific wavelength is shown. Left: $\lambda = 0.1$ m. Middle: $\lambda = 0.01$ m. Right: $\lambda = 0.001$ m. The symbol + marks the base state given by Table 2, and the symbol * marks the base state given by Table 3.

grow large, the assumptions made in the linearization of the model become invalid, and the behavior of the full model will depart from the behavior of the linearized model. At this point, the nonlinear stability of the model must be considered (López de Bertodano et al., 2017). Nonlinear effects can bound perturbations that grow initially due to linear instability. Typically, the unstable perturbations develop into shocks, which must be bounded by a dissipative mechanism. In Section 5.4 we show numerically that physical diffusion plays a crucial role in the nonlinear damping of linear instabilities that develop into shocks. At coarse grid resolutions, this role is taken over by numerical diffusion.

An analytical indication of a form of nonlinear stability, which the model should satisfy even when it is linearly unstable, is given by the energy conservation property. The extended local energy, given by (12), can be written in the following primitive form for the 2D channel geometry:

$$e_{\mathrm{ch}} = \frac{1}{2}\rho_U g_n H_U^2 + \rho_U g_n H_U H_L + \frac{1}{2}\rho_L g_n H_L^2 + \frac{1}{2}\rho_U u_U^2 H_U + \frac{1}{2}\rho_L u_L^2 H_L$$
$$+ \rho_U g y H_U + \rho_L g y H_L + \sigma\left(1 + \frac{1}{2}\left(\frac{\partial H_L}{\partial s}\right)^2\right). \quad (67)$$

Since H_U and H_L must be positive, each term in this expression is positive. Therefore the global energy equation (15) implies a bound

on the velocities, the heights, and their spatial derivatives. A numerical model that conserves (or strictly dissipates) this energy can be expected to have solutions that are bounded in this way.

In conclusion, the extended model linearly damps short wavelength perturbations, nonlinearly damps unstable long wavelength perturbations when they grow large, and possesses an energy bound. These properties are achieved by adding only physically derived terms to the basic model (physical diffusion, friction, and surface tension). The end result is a reliable model that can be expected to handle difficult flow states, while still resolving physical instabilities.

5. Numerical experiments

5.1. Introduction

In this section, the energy stability and well-posedness properties of our new framework are demonstrated through three different numerical experiments. These were conducted using a code based on the spatial discretizations given in Section 3. The numerical experiments consider a 2D channel geometry, for which the original advective flux described in Section 3.1 and the surface tension discretization described in Section 3.6 are exactly energy-conserving.

Table 4
Base state for the traveling wave case.

Variable	Symbol	Value	Units
Initial lower fluid hold-up	$\alpha_{L,0}$	0.5	–
Initial lower fluid velocity	$u_{L,0}$	0.5	$\mathrm{m\,s^{-1}}$
Initial upper fluid velocity	$u_{U,0}$	0.5	$\mathrm{m\,s^{-1}}$

For the time integration we use the fourth order constraint-consistent Runge–Kutta method described by Sanderse and Veldman (2019). This method is explicit for the mass and momentum equations and implicit for the pressure, requiring the solution of a pressure Poisson equation. It requires the mass and momentum equations to be coupled as has been done by setting the fluxes in the mass equations according to (37a).

First, in Section 5.2 we consider a traveling wave solution to the basic TFM without diffusion or surface tension. We show that our novel energy-stable advective flux (described in Section 3.8) yields smooth solutions without excessive numerical diffusion or numerical oscillations. We compare this flux to our original energy-conserving flux (described in Section 3.1) and to our strictly dissipative upwind flux (described in Section 3.7). Additionally, we compare these to a naive central scheme which is neither energy-conserving nor strictly dissipative.

In Section 5.3 we repeat the traveling wave case, but with surface tension added according to Section 3.6. We show that this addition is energy-conserving, as predicted by the analysis.

Last, in Section 5.4 we consider an unstable perturbation to a shear flow base state that would be ill-posed for the basic TFM. We demonstrate that the complete new framework with friction, diffusion, surface tension, and the energy-stable advective flux, is able to obtain solutions that converge with increasing grid resolution, for this challenging test case. We quantify the contributions of numerical diffusion, physical diffusion and friction to the nonlinear damping by computing the dissipation, using our derived expressions for the dissipation rates.

5.2. Traveling wave with the basic model and different advective fluxes

We conduct a test case with a traveling wave, induced as a perturbation upon a uniform base state, for the basic model without diffusion, friction, or surface tension. The base state is given in Table 4, and the flow parameters are those of Table 1. The perturbation is defined according to the analysis in Appendix C. It is the initial condition for the exact solution to the linearized system, for one of the two modes $\omega(k)$. We set the wavelength of the perturbation to $\lambda = 0.1$ m, and select the wave mode $\omega = 39.89\,\mathrm{s^{-1}}$ (the other option is $\omega = 22.94\,\mathrm{s^{-1}}$ and would yield a slower wave). The perturbation is then limited to the range between $s_{\mathrm{pert}} - \lambda/2$ and $s_{\mathrm{pert}} + \lambda/2$, with $s_{\mathrm{pert}} = 2\lambda + \lambda/4$. Outside of this range the base state is kept. The computational domain has length $L = 0.5$ and has periodic boundaries. A pressure projection step is performed on the complete initial condition, adjusting the velocities to ensure that the volumetric flow constraint is satisfied (see Sanderse and Veldman (2019)).

The exact solution of the linearized model is a wave traveling to the right without deformation. The solution to the full nonlinear model, using the energy-stable advective flux described in Section 3.8, is shown in Fig. 6. We show the hold-up $\alpha_L = A_L/A$ and the upper fluid velocity u_U. The wave travels to the right at constant velocity, with little deformation. At $t = 3.15$ s and $t = 6.30$ s, the wave has traveled through the domain an integer number of times (4 and 8 times respectively), and the wave can be compared to the initial perturbation. In the middle of the wave, a slight steepening has taken place, tending towards the formation of a discontinuity. At the edges, the wave has diffused slightly.

In Fig. 7, we compare results for this test case, using different discretizations of the advective flux in the momentum equations. We compare the energy-stable scheme given by (64), the upwind scheme given by (61), the energy-conserving scheme given in (37a), and a naive central interpolation scheme in which the momentum advection fluxes are given by

$$f_{3,a,i-1,\mathrm{cen}} = \left[\left(\frac{q_{3,i-1}}{\bar{q}_{1,i-1}}\right)\right]^2 \frac{q_{1,i-1}}{\Delta s} = \rho_U \left(\bar{u}_{U,i-1}\right)^2 A_{U,i-1},$$

$$f_{4,a,i-1,\mathrm{cen}} = \left[\left(\frac{q_{4,i-1}}{\bar{q}_{2,i-1}}\right)\right]^2 \frac{q_{2,i-1}}{\Delta s} = \rho_L \left(\bar{u}_{L,i-1}\right)^2 A_{L,i-1}.$$

A high-resolution solution ($\Delta s = 1.25 \cdot 10^{-4}$ m and $\Delta t = 1.25 \cdot 10^{-5}$ s), obtained using the energy-stable scheme, is used as a reference. The results show that the central and energy-conserving schemes produce numerical oscillations in the presence of strong gradients, while the upwind scheme is excessively diffusive. The proposed energy-stable scheme yields the most accurate solution, without numerical oscillations and with much less diffusion than the upwind scheme.

This behavior can be understood from the perspective of the (global) energy, of which Fig. 7 shows the absolute and nondimensional difference with respect to the initial condition. The energy-conserving scheme conserves energy up to a very small time integration error. The energy-stable and upwind schemes lose energy with respect to the initial condition, while the central scheme gains energy (this is not visible since only the absolute difference is plotted). The energy-stable scheme is less dissipative than the upwind scheme, which is reflected in its less diffused solution. Some dissipation is physically necessary near strong gradients or discontinuities, and the lack of this in the central and energy-conserving schemes can be understood to lead to numerical oscillations.

5.3. Traveling wave with surface tension

Adding surface tension to the basic model yields a model that is still energy-conserving, but for the modified energy $e = e_b + e_s$. We repeat the previous case with this model. We test the surface tension implementation described in Section 3.6 with the energy-conserving advective flux to show that the addition is energy-conserving. We also test the surface tension implementation with the energy-stable flux and show that practically this yields the best results.

The addition of surface tension results in a different angular frequency of $\omega = 40.19\,\mathrm{s^{-1}}$, for $\lambda = 0.1$ m (the other mode is $\omega = 22.64\,\mathrm{s^{-1}}$). The solution at various points in time is shown in Fig. 8. Due to the slightly increased wave speed, the snapshots at $t = 3.13$ s and 6.25 s are now the points at which the wave has traveled through the domain 4 and 8 times respectively. The addition of surface tension has a dispersive effect: the traveling wave spreads out into smaller oscillations, which are not of numerical origin. This can be determined from the fact that they do not vanish upon grid refinement.

Fig. 9 shows energy and convergence results using the energy-conserving advective flux. Using the energy-conserving advective flux makes it possible to isolate the effect of the surface tension implementation on the (global) energy. The figure shows how the total energy remains constant in time. This confirms our theoretical analysis: the surface tension implementation is indeed energy-conserving. The different components of the energy (potential, kinetic, and surface energy) are free to increase or decrease, exchanging with one another. The magnitude of the exchange is small.

Fig. 10 shows energy and convergence results using the energy-stable advective flux. Using this flux, the total energy is not conserved, but decreases monotonically, as discussed in Section 5.2. A comparison between the right plots of Figs. 9 and 10 shows that this comes with the advantages of smoother convergence and absence of numerical oscillations. Therefore the energy-stable flux is favored, in combination with the energy-conserving surface tension discretization.
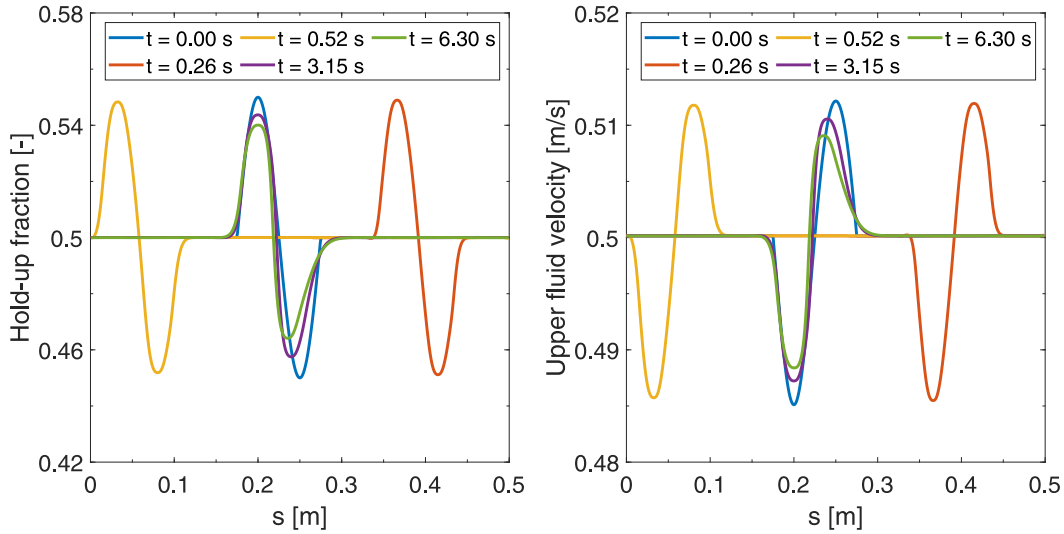
Fig. 6. Two components of the solution to the traveling wave case for the basic model, using the energy-stable advective flux described in Section 3.8, with $\Delta s = 10^{-3}$ m and $\Delta t = 10^{-4}$ s.
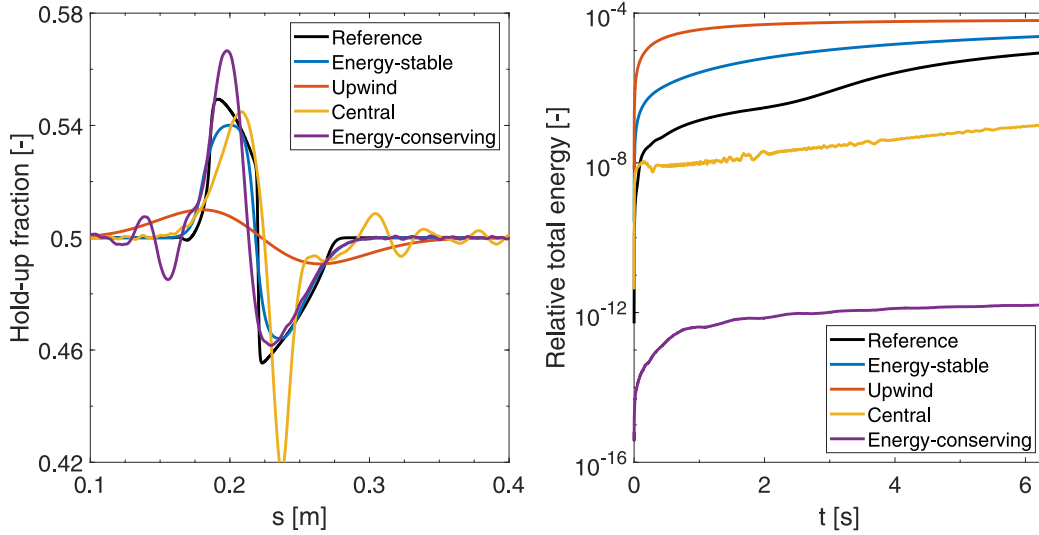

Fig. 7. Comparison of results of the traveling wave case for the basic model, using different advective flux discretizations. In all cases, $\Delta s = 10^{-3}$ m and $\Delta t = 10^{-4}$ s. The reference is a high-resolution solution ($\Delta s = 1.25 \cdot 10^{-4}$ m and $\Delta t = 1.25 \cdot 10^{-5}$ s) obtained using the energy-stable scheme. Left: the solution for the hold-up at time $t = 6.3$ s. Right: the absolute difference between the energy as a function of time and the initial energy, divided by the initial energy.

5.4. Shock formation and dissipation in unstable region

In this test case we test our complete proposed framework, with all physical effects and the energy-stable advective flux, on a challenging case involving the rapid growth of a perturbation and development into a shock. The flow is in the region of state space where the basic model is ill-posed: it is marked with the symbol $*$ in the stability maps of Section 4. However, with our extended model we are able to obtain good convergence and a well-resolved shock.

This test case is inspired by a case from Fullmer et al. (2014b), which is in turn derived from Holmås et al. (2008). The boundaries are periodic, the flow parameters are given by Table 1, and the base state is given by Table 3. This base state is altered by a single-period sinusoidal perturbation in the hold-up (with wavelength $\lambda = 0.1$ m and amplitude $\Delta \alpha_L = 0.05$), which determines the initial conditions for q_1 and q_2. The velocities are not explicitly perturbed. Instead, a pressure projection step is performed on the base state plus perturbed hold-up. The projection step perturbs the velocities such that the volumetric flow constraint is satisfied, yielding the initial conditions for q_3 and

q_4. Two components of the resulting initial condition (expressed in primitive variables) can be seen in Fig. 11, along with the evolution of the wave in time. The main difference between this case and the case from Fullmer et al. (2014b) is that we add wall and interface friction, so that all sources of dissipation are included in the numerical experiment. The friction is balanced by a driving pressure gradient, with a (constant) value given by Table 3, so that the base state is a steady state (see Section 4). Without the external forcing provided by a driving pressure gradient, the initial perturbation would quickly die out.

While the basic model possesses an unbounded short wave growth rate for these flow conditions, the extended model damps short wavelength perturbations (see Fig. 4). The wavelength of the perturbation considered here is still unstable, and indeed the perturbation is observed to grow rapidly in Fig. 11. Fortunately, as predicted by the linear stability analysis, it grows at a finite rate, and is not dominated by extreme short wavelength instabilities. Finally, after developing into a shock its growth is stopped by nonlinear effects. After this point, secondary perturbations will start to grow, which will continue
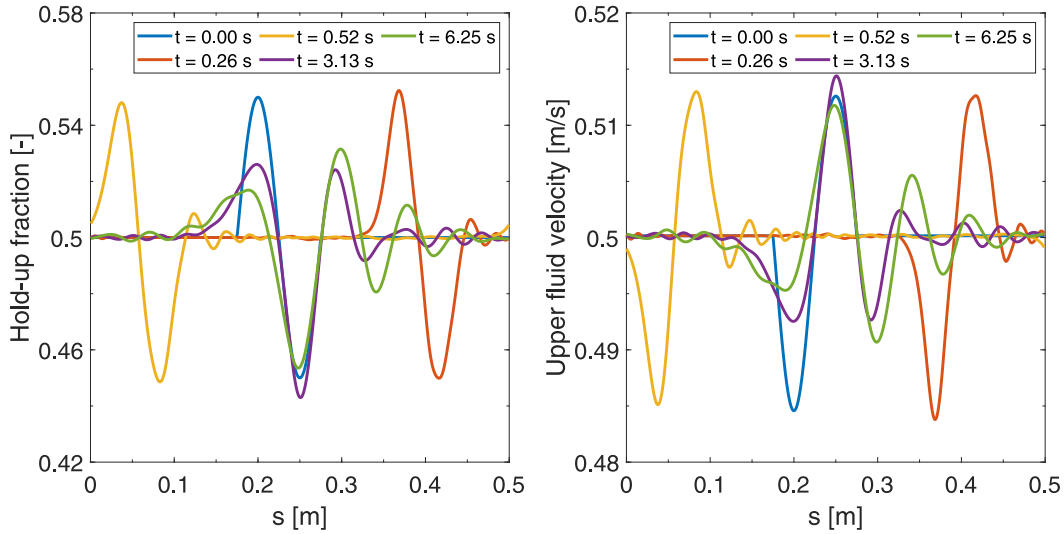
Fig. 8. Two components of the solution to the traveling wave case for the basic model plus surface tension, using the energy-stable advective flux, with $\Delta s = 10^{-3}$ m and $\Delta t = 10^{-4}$ s.
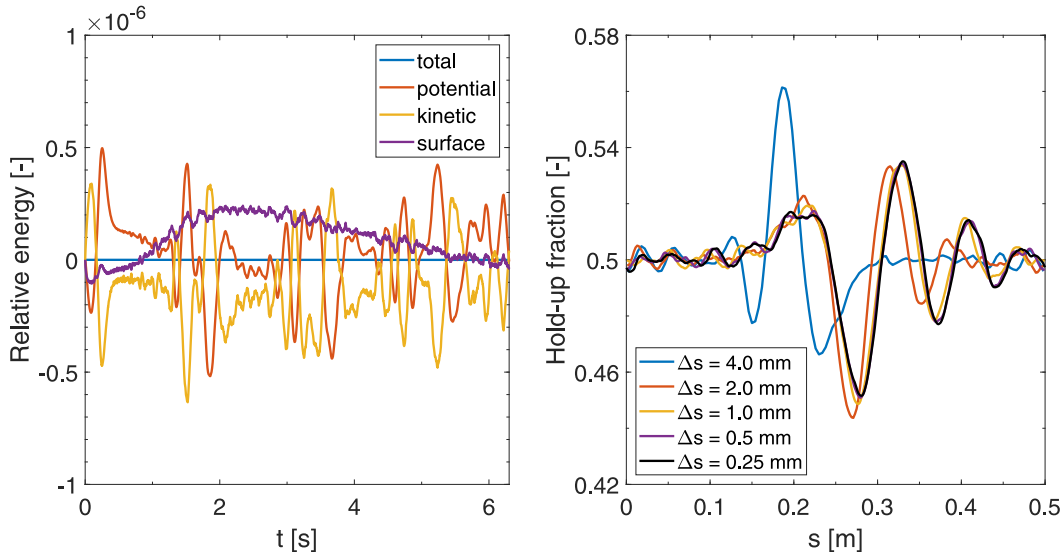

Fig. 9. Results for the traveling wave case with surface tension, using the energy-conserving advective flux. Left: components of the energy of the solution, with $\Delta s = 10^{-3}$ m and $\Delta t = 10^{-4}$ s. Right: convergence of the hold-up at time $t = 6.3$ s, with a constant ratio $\Delta t / \Delta s = 0.1$ s/m.

traveling to the right, through the periodic boundary, to reappear on the left side of the domain. The secondary perturbations also form discontinuities and remain bounded in the same manner as the primary perturbation. Eventually, at much later time, a sequence of roll waves is observed, as shown in Fig. 12.

The global dissipation as a function of time is shown in Fig. 13. Here the dissipated energy is calculated using the expressions for the local dissipation − $\epsilon_{d,i-1/2}$, $\epsilon_{f,i-1/2}$, $\epsilon_{n,i-1/2}$ − and the expression for energy production due to a driving pressure gradient − $c_{p,i-1/2}$. These expressions are summed over the domain and integrated in time (numerically) according to (49), and their sum yields the total dissipated energy. Since the initial base state is uniform, it has no (physical or numerical) diffusion, but it does have high dissipation due to friction which is balanced by an energy input from the driving pressure gradient. These base state dissipation and production terms have been subtracted so that friction and the driving pressure gradient do not dominate the plot.

In the second plot of Fig. 13, the instantaneous energy is calculated using the expression for $e_{i-1/2}$, summed over the domain to yield the global energy. The left and right plots of Fig. 13 show the same decrease in total energy, confirming that the two methods of calculation are consistent.

Fig. 13 reveals exactly how nonlinear effects bound the amplitude of the shock. The respective contributions of the physical and numerical diffusion to the nonlinear damping can now be quantified, by examining their effect on the energy of the solution. The figure shows that as the shock develops, the physical and numerical diffusion and their resulting dissipation grow large, and decrease the energy of the solution. They act to decrease the kinetic energy of the solution, allowing the potential and surface energy to grow slightly. We note that a calculation of the local dissipation shows the dissipation to be localized around the shock.

The dissipation due to friction also grows with time, but less dramatically, since it is proportional to the size of the wave, not to its steepness. It has a smaller stabilizing effect. Regarding the driving pressure gradient, the energy input remains roughly constant, since it is not dependent on the perturbation but only on the volumetric flow rate, which is a property of the complete flow. Its negative value at $t = 0.16$ s means that the energy input is slightly lower than it was for the initial base state, since the volumetric flow rate has decreased slightly, indicating that the flow has been slowed down slightly.

Fig. 14 shows how the solution converges with grid resolution, confirming that the extended model is well-posed, as discussed in
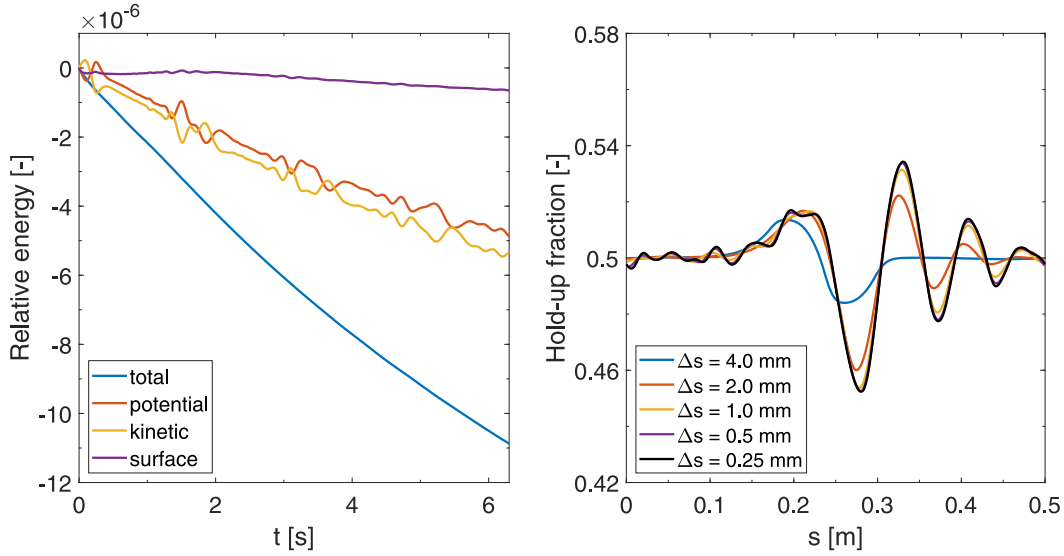
Fig. 10. Results for the traveling wave case with surface tension, using the energy-stable advective flux. Left: components of the energy of the solution, with $\Delta s = 10^{-3}$ m and $\Delta t = 10^{-4}$ s. Right: convergence of the hold-up at time $t = 6.3$ s, with a constant ratio $\Delta t / \Delta s = 0.1$ s/m.
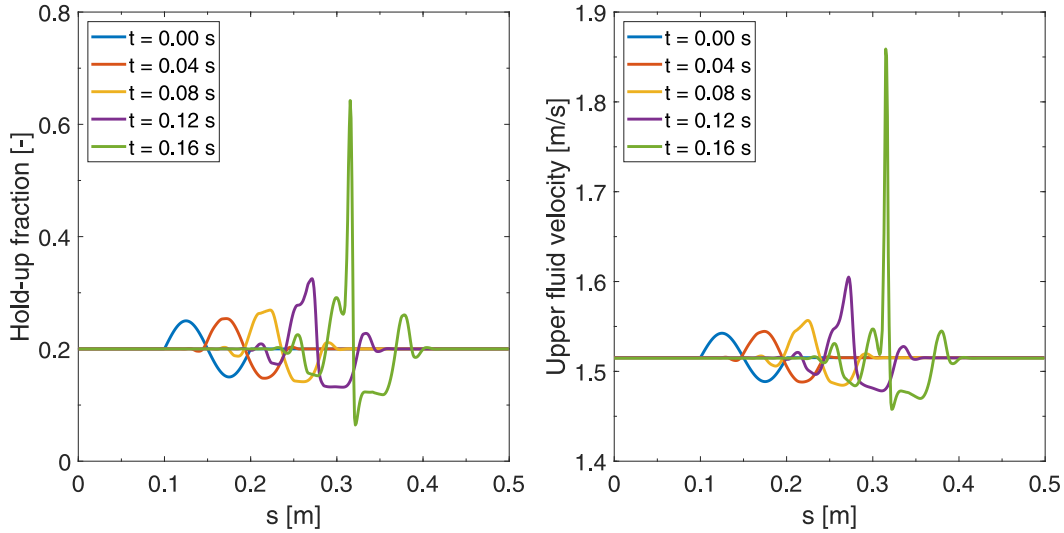

Fig. 11. Initial condition, and solution over time, for two components of the solution to the unstable shock formation case. Using the energy-stable advective flux, with $\Delta s = 10^{-3}$ m and $\Delta t = 10^{-4}$ s.

Section 4. Also shown in Fig. 14 is the convergence of the dissipation, divided into its different components. As the grid is refined, the small scales at which the physical diffusion acts are better resolved, allowing the corresponding dissipation to grow and converge to its full physical effect. In contrast, beyond a certain resolution before which the solution is relatively smooth, the numerical dissipation decreases with grid resolution. Only at coarse resolutions, numerical dissipation is needed to compensate for the lack of physical dissipation. Dissipation due to friction only varies slightly with grid resolution, since it is not a small scale phenomenon.

Previous work has described how the linearly unstable wave is bounded by (nonlinear) dissipation in the shock, due to numerical and physical diffusion (Fullmer et al., 2014b). However, up to now, dissipation has remained an abstract concept for the TFM. Here we provide definitions for the various components of the dissipation, and specify their effect on a well-defined energy. Therefore, dissipation has become a concrete quantity that can be measured. This provides a stronger basis for discussions of the nonlinear damping of unstable waves. We confirm the conclusions of Fullmer et al. (2014b), who observe that with only

numerical diffusion, the solution fails to converge (with oscillations appearing at high resolutions), due to the lack of numerical diffusion at high grid resolutions. We similarly observe (results not shown here) that physical diffusion without numerical diffusion leads to a less clear convergence, with coarse grid solutions being insufficiently diffused. With Fig. 14 we have made concrete that with a combination of numerical and physical diffusion, the dissipation in the shock smoothly converges to a finite value, realizing a grid-independent bound on the amplitude of the shock.

6. Conclusions

This paper has proposed a complete energy-stable framework – including diffusion, friction, surface tension, and an energy-stable advective flux scheme – for reliable simulations with the one-dimensional two-fluid model (TFM). The paper builds on our earlier work on the energy-conserving basic TFM, which we have extended in an energy-consistent manner. We have shown that for the channel geometry, surface tension can be added to the model in an energy-conserving
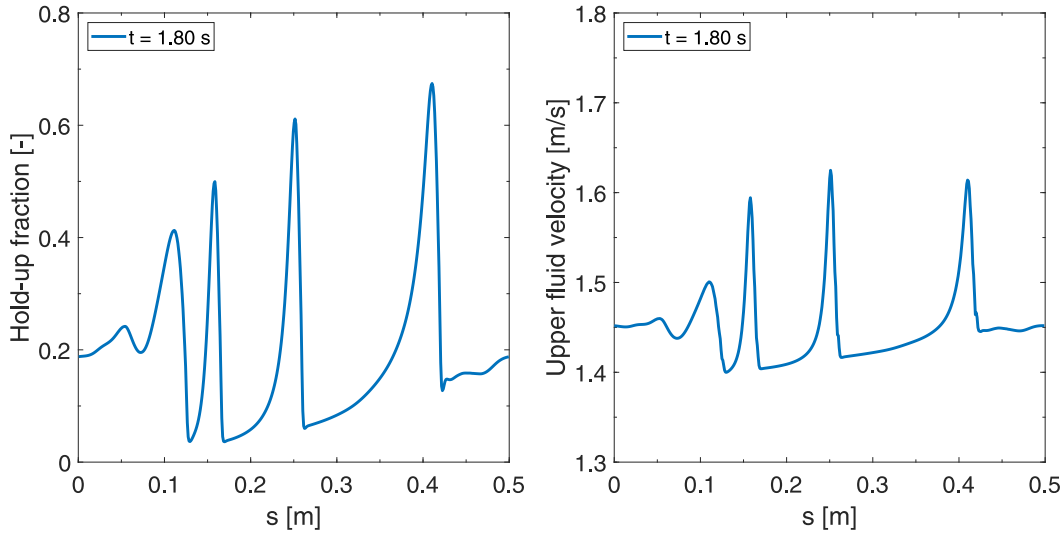
Fig. 12. Snapshot of two components of the solution to the unstable shock formation case, at time $t = 1.8$ s. Using the energy-stable advective flux, with $\Delta s = 10^{-3}$ m and $\Delta t = 10^{-4}$ s. This figure shows how after the rapid growth depicted in Fig. 11, the shock breaks up into several roll waves that remain of limited amplitude.
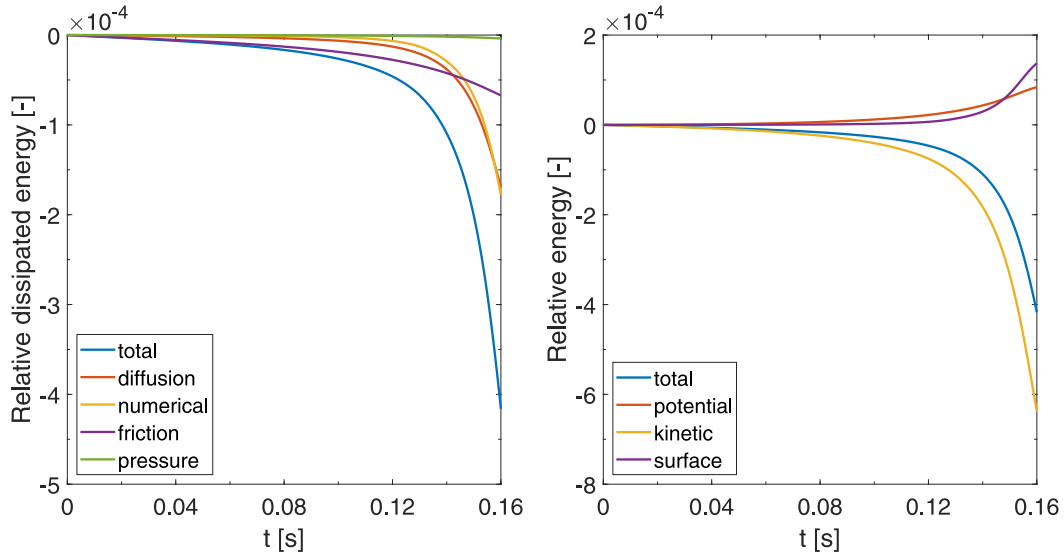

Fig. 13. For the unstable shock formation case, this figure shows the dissipated energy (left) and the instantaneous energy (right), made non-dimensional by the total energy of the initial condition. Using the energy-stable advective flux, with $\Delta s = 10^{-3}$ m and $\Delta t = 10^{-4}$ s. The total dissipation is divided into contributions from physical diffusion, numerical diffusion, wall and interface friction, and a production term due to an externally applied driving pressure gradient.

manner. The additions of friction and momentum diffusion have been shown to be strictly dissipative. Therefore, these extensions yield an energy-stable model.

Besides their implications for energy stability, the additions to the model also solve the basic model's issue of unbounded linear instability at short wavelengths: diffusion and surface tension introduce a cut-off wavelength below which perturbations are damped. The cut-off wavelength is shown to depend on the state: it decreases with increasing velocity difference between the phases. Nevertheless, there exists a cut-off wavelength for any state, rendering the model unconditionally well-posed. These cut-off wavelengths may be shorter than the scales at which the TFM is usually employed, but it is these scales at which the ill-posedness issue of the one-dimensional model resides and it is these scales which need to be stabilized. Diffusion and surface tension offer a clearly physically motivated way to do so. Precisely because diffusion and surface tension are physically motivated, they fit well into our energy-stable framework.

The energy conservation and dissipation properties of the model have been proven to carry over to the semi-discrete model, when the model and its energy are discretized in a specific manner. The semi-discrete model with surface tension is exactly energy-conserving, if the surface energy is added to the basic energy as an extra term. Diffusion and friction add strictly dissipative terms to the local energy conservation equation, with expressions for the dissipation rates that can be evaluated as functions of the local instantaneous solution.

However, the key highlight of our semi-discrete model is a new discretization of the advective terms, which combines a previously developed energy-conserving central discretization and a strictly dissipative upwind discretization. These discretizations are combined using flux limiters. The novel combined advective flux is energy stable, and comes with an explicit expression for the numerical dissipation rate, that can be evaluated during a numerical simulation. It is designed to be energy-conserving where the solution is smooth, and dissipative where the solution has strong gradients. This dissipation is motivated by the fact that the energy conservation property of the continuous model does not hold for discontinuous solutions: dissipation is required in this case. The novel energy-stable flux retains the advantages in stability
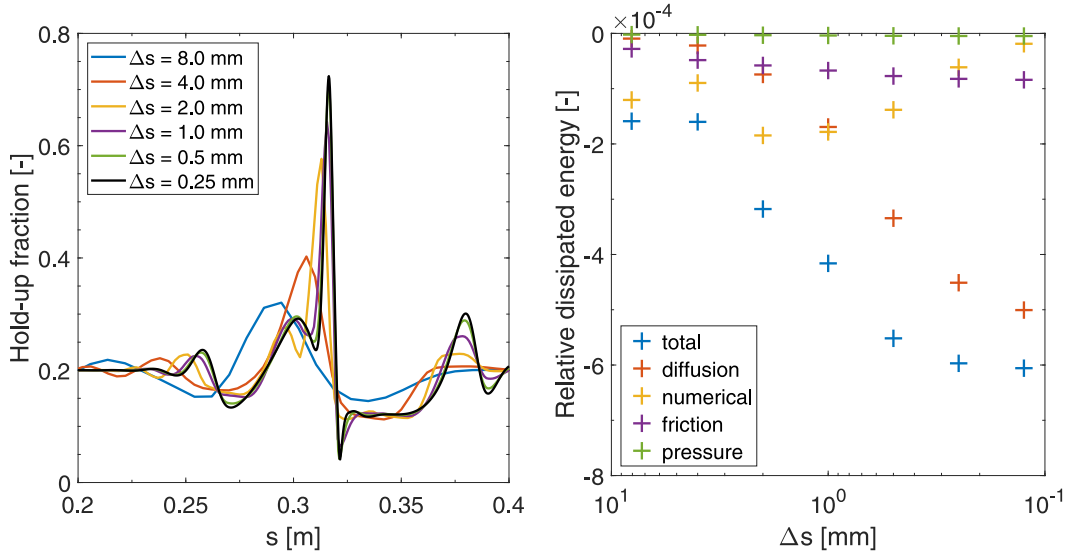
Fig. 14. For the unstable shock formation case, this figure shows the convergence with grid resolution, of the solution at time $t = 0.16\,\text{s}$. Using the energy-stable advective flux, with a constant ratio $\Delta t / \Delta s = 0.1\,\text{s/m}$. Left: hold-up fraction $\alpha_L = A_L / A$. Right: dissipated energy, divided by the total energy of the initial condition.

and physical fidelity of the original energy-conserving flux, without the latter's tendency to generate numerical oscillations near discontinuities.

In numerical experiments, spatially exact energy conservation is demonstrated for the basic model extended with surface tension, using the original energy-conserving flux. The upwind and energy-stable advective fluxes are demonstrated to be strictly dissipative, as opposed to a naive central discretization that is neither conservative nor strictly dissipative. The energy-stable scheme is shown to yield smooth solutions without numerical oscillations. It is much less diffusive than a first-order upwind scheme, and this is reflected in the dissipation, which is lower for the energy-stable scheme than for the upwind scheme.

A challenging test of our complete framework is provided by the simulation of an unstable wave in a region of state space where the basic model is linearly ill-posed. Our proposed framework yields a convergent solution, confirming that it is well-posed. The unstable perturbation develops into a shock, which is bounded by nonlinear dissipation. The analytical results of this work enable a precise analysis of the dissipation and better insight into the nonlinear damping taking place. The dissipation due to numerical and physical diffusion are observed to grow as the wave steepens, with numerical dissipation dominating at coarse resolutions and physical dissipation dominating at fine resolutions. Together, numerical and physical diffusion yield a smoothly converging total dissipation, and a smoothly converging solution.

In order to resolve the full effect of the physical diffusion and surface tension and reach convergence, the grid needs to be refined to high resolutions that may be impractical in engineering applications. When the additional computational expense associated with high resolutions is unwanted, our model has the advantage that it can also be used at coarse resolutions, where it provides solutions that are similar to the converged solutions, except that sharp perturbations are diffused. The convergence plots show a monotonic steepening of the waves, without spurious oscillations.

Though the semi-discrete computational model proposed in this paper is by itself no more computationally expensive than standard discretizations of the basic model, the inclusion of surface tension does place an additional restriction on the time step set in the explicit time integration method. For the basic model the time step only has to satisfy a CFL condition, giving the time step a bound that scales linearly with grid resolution. The addition of surface tension results in a higher order restriction, with an exponent between 1 and 2. Therefore, the

addition of surface tension increases the computational effort required for the fully discrete computational model, particularly at higher grid resolutions.

CRediT authorship contribution statement

J.F.H. Buist: Conceptualization, Formal analysis, Investigation, Software, Writing – original draft. **B. Sanderse:** Conceptualization, Software, Writing – review & editing. **S. Dubinkina:** Writing – review & editing. **C.W. Oosterlee:** Writing – review & editing. **R.A.W.M. Henkes:** Writing – review & editing.

Declaration of competing interest

The authors declare the following financial interests/personal relationships which may be considered as potential competing interests: J.F.H. Buist reports financial support was provided by Dutch Research Council. If there are other authors, they declare that they have no known competing financial interests or personal relationships that could have appeared to influence the work reported in this paper.

Data availability

Data will be made available on request.

Appendix A. Geometric relations

The equations are written in terms of the cross-sectional areas occupied by each fluid, which in general can be defined to be related to the interface height H_L via

$$A_L = \int_0^{H_L} w(h)\, \mathrm{d}h, \qquad A_U = \int_{H_L}^{H} w(h)\, \mathrm{d}h, \tag{A.1}$$

with $w(h)$ the local duct width. Note that $w(H_L) = P_{\text{int}}$, where P_{int} is the (generalized) interface perimeter which is shown for a circular pipe

geometry in Fig. 1. For the 2D channel geometry, $w(h) = 1$, and the cross-sections A_L and A_U are identical to the fluid heights H_L and H_U.

The geometric quantities $\widehat{H}_L$ and $\widehat{H}_U$ which appear in the governing equations of the two-fluid model, also have general definitions:

$$\widehat{H}_L := \int_0^{H_L} (h - H_L)w(h)\,\mathrm{d}h, \qquad \widehat{H}_U := \int_{H_L}^H (h - H_L)w(h)\,\mathrm{d}h. \quad (A.2)$$

Besides $\widehat{H}_L$ and $\widehat{H}_U$, the following geometric quantities are used in the energy definition:

$$\begin{aligned} \widetilde{H}_L &:= \int_0^{H_L} h w(h)\,\mathrm{d}h = \widehat{H}_L + H_L A_L, \\ \widetilde{H}_U &:= \int_{H_L}^H h w(h)\,\mathrm{d}h = \widehat{H}_U + (H - H_U)A_U. \end{aligned} \quad (A.3)$$

We can apply Leibniz' rule to (A.1) (see Buist et al. (2022)) to obtain

$$\frac{\mathrm{d}A_L}{\mathrm{d}H_L} = P_{\text{int}}, \qquad \frac{\mathrm{d}A_U}{\mathrm{d}H_U} = P_{\text{int}},$$

where we have used $H_L + H_U = H$. Applying the same technique to (A.2) and (A.3) yields

$$\begin{aligned} \frac{\mathrm{d}\widehat{H}_L}{\mathrm{d}H_L} &= -A_L, & \frac{\mathrm{d}\widehat{H}_U}{\mathrm{d}H_U} &= A_U, \\ \frac{\mathrm{d}\widetilde{H}_L}{\mathrm{d}H_L} &= H_L P_{\text{int}}, & \frac{\mathrm{d}\widetilde{H}_U}{\mathrm{d}H_U} &= (H - H_U)P_{\text{int}}, \end{aligned}$$

which leads to

$$\frac{\mathrm{d}\widehat{H}_L}{\mathrm{d}A_L} = \frac{\mathrm{d}\widehat{H}_L}{\mathrm{d}H_L}\left[\frac{\mathrm{d}A_L}{\mathrm{d}H_L}\right]^{-1} = -\frac{A_L}{P_{\text{int}}}, \quad \frac{\mathrm{d}\widehat{H}_U}{\mathrm{d}A_U} = \frac{\mathrm{d}\widehat{H}_U}{\mathrm{d}H_U}\left[\frac{\mathrm{d}A_U}{\mathrm{d}H_U}\right]^{-1} = \frac{A_U}{P_{\text{int}}}, \quad (A.4)$$

$$\frac{\mathrm{d}\widetilde{H}_L}{\mathrm{d}A_L} = \frac{\mathrm{d}\widetilde{H}_L}{\mathrm{d}H_L}\left[\frac{\mathrm{d}A_L}{\mathrm{d}H_L}\right]^{-1} = H_L, \quad \frac{\mathrm{d}\widetilde{H}_U}{\mathrm{d}A_U} = \frac{\mathrm{d}\widetilde{H}_U}{\mathrm{d}H_U}\left[\frac{\mathrm{d}A_U}{\mathrm{d}H_U}\right]^{-1} = H - H_U. \quad (A.5)$$

A similar calculation, in which we assume that H is constant, yields

$$\frac{\partial \widehat{H}_L}{\partial s} = -A_L \frac{\partial H_L}{\partial s}, \qquad \frac{\partial \widehat{H}_U}{\partial s} = -A_U \frac{\partial (H - H_U)}{\partial s}.$$

Finally, comparison to (A.5) yields

$$\frac{\partial \widehat{H}_L}{\partial s} = -A_L \frac{\partial}{\partial s}\left(\frac{\mathrm{d}\widetilde{H}_L}{\mathrm{d}A_L}\right), \qquad \frac{\partial \widehat{H}_U}{\partial s} = -A_U \frac{\partial}{\partial s}\left(\frac{\mathrm{d}\widetilde{H}_U}{\mathrm{d}A_U}\right), \quad (A.6)$$

and these geometric relations are critical to deriving the local energy conservation equation.

The general geometric quantities $\widehat{H}_L$ and $\widehat{H}_U$ can be evaluated for specific geometries. For a 2D channel geometry, (A.2) evaluates to

$$\widehat{H}_L = -\frac{1}{2}H_L^2, \qquad \widehat{H}_U = \frac{1}{2}H_U^2,$$

where we have substituted $H_L = H - H_U$. For the pipe geometry, the results of the integrals are given by (Sanderse et al., 2017):

$$\widehat{H}_L = \left[(R - H_L)A_L - \frac{1}{12}P_{\text{int}}^3\right], \qquad \widehat{H}_U = -\left[(R - H_U)A_U - \frac{1}{12}P_{\text{int}}^3\right].$$

The general geometric quantities that appear in the energy definition also have specific forms for different geometries. For the channel geometry, the general expressions (A.3) evaluate to

$$\widetilde{H}_L = \frac{1}{2}H_L^2, \qquad \widetilde{H}_U = \frac{1}{2}H_U^2 + H_U H_L.$$

For the pipe geometry the results are

$$\widetilde{H}_L = \left[RA_L - \frac{1}{12}P_{\text{int}}^3\right], \qquad \widetilde{H}_U = \left[RA_U + \frac{1}{12}P_{\text{int}}^3\right].$$

Appendix B. Friction closure relations

The wall and interface stresses of the two-fluid model are typically modeled in the following manner (Taitel and Dukler, 1976):

$$\tau_L = -\frac{1}{2}f_L \rho_L u_L |u_L|, \qquad \tau_U = -\frac{1}{2}f_U \rho_U u_U |u_U|,$$

$$\tau_{\text{int}} = -\frac{1}{2}f_{\text{int}}\rho_U\left(u_U - u_L\right)|u_U - u_L|,$$

in which f_L, f_U, and f_{int} are the Fanning friction factors, which require further closure relations. The friction factors depend on the Reynolds numbers

$$\mathrm{Re}_L = \frac{|u_L|D_L}{\nu_{m,L}}, \qquad \mathrm{Re}_U = \frac{|u_U|D_U}{\nu_{m,U}},$$

with hydraulic diameters

$$D_L = \frac{4A_L}{P_L}, \qquad D_U = \frac{4A_U}{P_U + P_{\text{int}}}.$$

In this work we use the Taitel and Dukler friction model (Barnea and Taitel, 1993; Taitel and Dukler, 1976)

$$f_L = \frac{C}{\mathrm{Re}_L^n}, \qquad f_U = \frac{C}{\mathrm{Re}_U^n}, \qquad f_{\text{int}} = \max\left(f_U, 0.014\right),$$

with coefficients $C = 0.046$ and $n = 0.2$ (valid for turbulent flow).

Appendix C. Linear stability analysis

We conduct a linear stability analysis of the (continuous) model, following Fullmer et al. (2014b), Liao et al. (2008) and López de Bertodano et al. (2017). The analysis starts by writing (10) in quasilinear matrix form, which can be done by substituting the volume constraint and assuming the solution is smooth:

$$\mathbf{A}(\mathbf{w})\frac{\partial \mathbf{w}}{\partial t} + \mathbf{B}(\mathbf{w})\frac{\partial \mathbf{w}}{\partial s} + \mathbf{E}(\mathbf{w})\frac{\partial^2 \mathbf{w}}{\partial s^2} + \mathbf{G}(\mathbf{w})\frac{\partial^3 \mathbf{w}}{\partial s^3} = \mathbf{c}(\mathbf{w}), \quad (C.1)$$

with

$$\mathbf{w} = \begin{bmatrix} w_1 \\ w_2 \\ w_3 \\ w_4 \end{bmatrix} = \begin{bmatrix} A_L \\ u_L \\ u_U \\ p \end{bmatrix}, \qquad \mathbf{A} = \begin{bmatrix} 1 & 0 & 0 & 0 \\ -1 & 0 & 0 & 0 \\ 0 & 1 & 0 & 0 \\ 0 & 0 & 1 & 0 \end{bmatrix},$$

$$\mathbf{B} = \begin{bmatrix} w_2 & w_1 & 0 & 0 \\ -w_3 & 0 & A - w_1 & 0 \\ -\frac{g_n}{w_1}\frac{\mathrm{d}\widehat{H}_L}{\mathrm{d}A_L} & w_2 - \frac{1}{w_1}\frac{\partial}{\partial s}\left(\nu_{\text{eff},L}w_1\right) & 0 & 1/\rho_L \\ \frac{g_n}{A-w_1}\frac{\mathrm{d}\widehat{H}_U}{\mathrm{d}A_U} & 0 & w_3 - \frac{1}{A-w_1}\frac{\partial}{\partial s}\left(\nu_{\text{eff},U}(A-w_1)\right) & 1/\rho_U \end{bmatrix},$$

$$\mathbf{c} = \begin{bmatrix} 0 \\ 0 \\ -\frac{1}{\rho_L}\frac{\partial p_{\text{body}}}{\partial s} + \frac{\tau_L P_L}{\rho_L w_1} - \frac{\tau_{\text{int}} P_{\text{int}}}{\rho_L w_1} - g_s \\ -\frac{1}{\rho_U}\frac{\partial p_{\text{body}}}{\partial s} + \frac{\tau_U P_U}{\rho_U (A-w_1)} + \frac{\tau_{\text{int}} P_{\text{int}}}{\rho_U (A-w_1)} - g_s \end{bmatrix},$$

$$\mathbf{E} = \begin{bmatrix} 0 & 0 & 0 & 0 \\ 0 & 0 & 0 & 0 \\ \frac{\sigma}{\rho_L}\frac{1}{P_{\text{int}}^2}\frac{\mathrm{d}P_{\text{int}}}{\mathrm{d}A_L}\frac{\partial w_1}{\partial s} & -\nu_{\text{eff},L} & 0 & 0 \\ 0 & 0 & -\nu_{\text{eff},U} & 0 \end{bmatrix},$$

$$\mathbf{G} = \begin{bmatrix} 0 & 0 & 0 & 0 \\ 0 & 0 & 0 & 0 \\ -\frac{\sigma}{\rho_L}\frac{1}{P_{\text{int}}} & 0 & 0 & 0 \\ 0 & 0 & 0 & 0 \end{bmatrix}.$$

Here we have used the second expression in (26) for the surface tension, which can be applied to both the 2D channel and the circular pipe geometries.

A general method for the linearization of systems of quasilinear partial differential equations is given by Prosperetti and Tryggvason (2007). The general solution is decomposed into $\mathbf{w} = \bar{\mathbf{w}} + \Delta\mathbf{w}$ with $\Delta\mathbf{w}$ a small disturbance ($\Delta\mathbf{w} \ll \bar{\mathbf{w}}$), and $\bar{\mathbf{w}}$ a base state that is itself also a solution to the equations. Additionally, we assume that the base state is a uniform steady state (its derivatives to s and to t are zero). Then, neglecting terms that are higher order in $\Delta\mathbf{w}$, and subtracting the

equation for the base state (which is satisfied by definition), a system of the form (C.1) can be approximated by

$$\mathbf{A}(\bar{\mathbf{w}})\frac{\partial \Delta \mathbf{w}}{\partial t} + \mathbf{B}(\bar{\mathbf{w}})\frac{\partial \Delta \mathbf{w}}{\partial s} + \mathbf{E}(\bar{\mathbf{w}})\frac{\partial^2 \Delta \mathbf{w}}{\partial s^2} + \mathbf{G}(\bar{\mathbf{w}})\frac{\partial^3 \Delta \mathbf{w}}{\partial s^3} = \mathbf{D}_C(\bar{\mathbf{w}})\Delta \mathbf{w}, \qquad (C.2)$$

with

$$\mathbf{D}_C(\bar{\mathbf{w}}) = \frac{\partial \mathbf{c}(\bar{\mathbf{w}})}{\partial \bar{\mathbf{w}}}.$$

Here, $\mathbf{D}_C$ is a Jacobian matrix. Due to the assumption of the uniform base state, and the neglecting of higher order terms, the terms in $\mathbf{B}(\bar{\mathbf{w}})$ and $\mathbf{E}(\bar{\mathbf{w}})$ involving partial derivatives to s drop out.

We write $\Delta \mathbf{w}$ as a Fourier series and substitute an arbitrary Fourier mode

$$\Delta \mathbf{w} = \Delta \hat{\mathbf{w}} \exp\left[i\left(ks - \omega t\right)\right],$$

with $\Delta \hat{\mathbf{w}}$ the amplitude, k the wavenumber, and ω the angular frequency, into (C.2). This yields the following linear system (Fullmer et al., 2014b):

$$\left[-\omega \mathbf{A}(\bar{\mathbf{w}}) + k\mathbf{B}(\bar{\mathbf{w}}) + i\mathbf{D}(\bar{\mathbf{w}}) + ik^2 \mathbf{E}(\bar{\mathbf{w}}) - k^3 \mathbf{G}(\bar{\mathbf{w}})\right]\Delta \hat{\mathbf{w}} = \mathbf{0}. \qquad (C.3)$$

For nontrivial solutions to exist, the determinant of the term between brackets must be zero, and solving for this yields two dispersion relations $\omega(k)$.

The perturbation amplitudes $\Delta \hat{\mathbf{w}}$ corresponding to the found dispersion relations can be found by substituting these in (C.3) and solving for $\Delta \hat{\mathbf{w}}$. This can be understood as, for each dispersion relation, finding the null space of the term between brackets in (C.3), which will consist of one vector. The associated phase angles can be calculated component-wise:

$$\theta = \arctan\left[\text{Im}(\Delta \hat{\mathbf{w}})/\text{Re}(\Delta \hat{\mathbf{w}})\right],$$

where each component of θ has a range $[-\pi, \pi]$ (use the four-quadrant inverse tangent).

This makes it possible to write the evolution in time of a perturbation as

$$\Delta \mathbf{w} = \sum_j \left|\Delta \hat{\mathbf{w}}_j\right| e^{\text{Im}\{\omega_j\}t} \cos\left(ks - \text{Re}\left\{\omega_j\right\}t + \theta_j\right), \qquad (C.4)$$

where we take the sum over the different solutions for ω for a given k, and the associated amplitude vectors. If a sinusoidal perturbation is initialized with a given wavenumber k, and an amplitude vector exactly corresponding to one of the two angular frequencies $\omega(k)$, then the sum in (C.4) can be left out and the perturbation will propagate as a single wave with speed $\text{Re}\{\omega\}$ and growth rate $\text{Im}\{\omega\}$. This holds exactly for the linearized system, but solutions to the full nonlinear system will deviate from this solution over time.

References

Aursand, P., Hammer, M., Munkejord, S.T., Wilhelmsen, Ø., 2013. Pipeline transport of CO2 mixtures: models for transient simulation. Int. J. Greenh. Gas Control 15, 174–185. http://dx.doi.org/10.1016/j.ijggc.2013.02.012.

Barnea, D., Taitel, Y., 1993. Kelvin-Helmholtz stability criteria for stratified flow: Viscous versus non-viscous (inviscid) approaches. Int. J. Multiph. Flow 19 (4), 639–649. http://dx.doi.org/10.1016/0301-9322(93)90092-9.

Barnea, D., Taitel, Y., 1994. Interfacial and structural stability of separated flow. Int. J. Multiph. Flow 20, 387–414. http://dx.doi.org/10.1016/0301-9322(94)90078-7.

Berry, R.A., Zou, L., Zhao, H., Zhang, H., Peterson, J.W., Martineau, R.C., Kadioglu, S.Y., Andrs, D., 2014. RELAP-7 Theory Manual. Technical Report INL/EXT-14-31366, Idaho National Laboratory, USA.

Bestion, D., 1990. The physical closure laws in the CATHARE code. Nucl. Eng. Des. 124 (3), 229–245. http://dx.doi.org/10.1016/0029-5493(90)90294-8.

Bonzanini, A., Picchi, D., Poesio, P., 2017. Simplified 1D incompressible two-fluid model with artificial diffusion for slug flow capturing in horizontal and nearly horizontal pipes. Energies 10 (9), 1372. http://dx.doi.org/10.3390/en10091372.

Bouchut, F., Morales de Luna, T., 2008. An entropy satisfying scheme for two-layer shallow water equations with uncoupled treatment. ESAIM Math. Model. Numer. Anal. 42 (4), 683–698. http://dx.doi.org/10.1051/m2an:2008019.

Buist, J.F.H., Sanderse, B., Dubinkina, S., Henkes, R.A.W.M., Oosterlee, C.W., 2022. Energy-conserving formulation of the two-fluid model for incompressible two-phase flow in channels and pipes. Comput. & Fluids 244, 105533. http://dx.doi.org/10.1016/j.compfluid.2022.105533.

Buist, J.F.H., Sanderse, B., Dubinkina, S., Oosterlee, C.W., Henkes, R.A.W.M., 2023. Energy-consistent formulation of the pressure-free two-fluid model. Internat. J. Numer. Methods Fluids 95 (5), 869–898. http://dx.doi.org/10.1002/fld.5168.

Castro, M.J., Fjordholm, U.S., Mishra, S., Parés, C., 2013. Entropy conservative and entropy stable schemes for nonconservative hyperbolic systems. SIAM J. Numer. Anal. 51 (3), 1371–1391. http://dx.doi.org/10.1137/110845379.

Chahed, J., Roig, V., Masbernat, L., 2003. Eulerian–Eulerian two-fluid model for turbulent gas–liquid bubbly flows. Int. J. Multiph. Flow 29 (1), 23–49. http://dx.doi.org/10.1016/S0301-9322(02)00123-4.

Dinh, T.N., Nourgaliev, R.R., Theofanous, T.G., 2003. Understanding the ill-posed two-fluid model. In: Proceedings of the 10th International Topical Meeting on Nuclear Reactor Thermal Hydraulics. NURETH-10, Seoul, Korea.

Drew, D.A., Passman, S.L., 1999. Theory of Multicomponent Fluids. Springer, New York.

Evje, S., Flåtten, T., 2003. Hybrid flux-splitting schemes for a common two-fluid model. J. Comput. Phys. 192 (1), 175–210. http://dx.doi.org/10.1016/j.jcp.2003.07.001.

Fabre, J., 2003. Gas-liquid slug flow. In: Bertola, V. (Ed.), Modelling and Experimentation in Two-Phase Flow. Springer, Vienna, pp. 117–156. http://dx.doi.org/10.1007/978-3-7091-2538-0_3.

Fjordholm, U.S., Mishra, S., Tadmor, E., 2009. Energy preserving and energy stable schemes for the shallow water equations. In: Cucker, F., Pinkus, A., Todd, M.J. (Eds.), Foundations of Computational Mathematics, Hong Kong 2008. Cambridge University Press, pp. 93–139. http://dx.doi.org/10.1017/CBO9781139107068.005.

Fjordholm, U.S., Mishra, S., Tadmor, E., 2011. Well-balanced and energy stable schemes for the shallow water equations with discontinuous topography. J. Comput. Phys. 230 (14), 5587–5609. http://dx.doi.org/10.1016/j.jcp.2011.03.042.

Fullmer, W.D., Lee, S.Y., Lopez de Bertodano, M.A., 2014a. An artificial viscosity for the ill-posed one-dimensional incompressible two-fluid model. Nucl. Technol. 185 (3), 296–308. http://dx.doi.org/10.13182/NT13-66.

Fullmer, W., Lopez de Bertodano, M., Ransom, V.H., 2011. The Kelvin-Helmholtz instability: Comparisons of one- and two-dimensional simulations. In: Proceedings of the 14th International Topical Meeting on Nuclear Reactor Thermal Hydraulics. NURETH-14, Toronto, Canada.

Fullmer, W.D., Ransom, V.H., Lopez de Bertodano, M.A., 2014b. Linear and nonlinear analysis of an unstable, but well-posed, one-dimensional two-fluid model for two-phase flow based on the inviscid Kelvin–Helmholtz instability. Nucl. Eng. Des. 268, 173–184. http://dx.doi.org/10.1016/j.nucengdes.2013.04.043.

Gassner, G.J., Winters, A.R., Kopriva, D.A., 2016. A well balanced and entropy conservative discontinuous Galerkin spectral element method for the shallow water equations. Appl. Math. Comput. 272, 291–308. http://dx.doi.org/10.1016/j.amc.2015.07.014.

Goldszal, A., Danielson, T.J., Bansal, K.M., Yang, Z.L., Johansen, S.T., Depay, G., 2007. LedaFlow 1D: Simulation results with multiphase gas/condensate and oil/gas field data. In: Proceedings of the 13th International Conference on Multiphase Production Technology. Edinburgh, United Kingdom, pp. 17–31.

Holmås, H., Sira, T., Nordsveen, M., Langtangen, H.P., Schulkes, R., 2008. Analysis of a 1D incompressible two-fluid model including artificial diffusion. IMA J. Appl. Math. 73 (4), 651–667. http://dx.doi.org/10.1093/imamat/hxm066.

Ishii, M., Mishima, K., 1984. Two-fluid model and hydrodynamic constitutive relations. Nucl. Eng. Des. 82, 107–126. http://dx.doi.org/10.1016/0029-5493(84)90207-3.

Issa, R.I., Kempf, M.H.W., 2003. Simulation of slug flow in horizontal and nearly horizontal pipes with the two-fluid model. Int. J. Multiph. Flow 29 (1), 69–95. http://dx.doi.org/10.1016/S0301-9322(02)00127-1.

Jameson, A., 2008. The construction of discretely conservative finite volume schemes that also globally conserve energy or entropy. J. Sci. Comput. 34 (2), 152–187. http://dx.doi.org/10.1007/s10915-007-9171-7.

Jones, A.V., Prosperetti, A., 1985. On the suitability of first-order differential models for two-phase flow prediction. Int. J. Multiph. Flow 11 (2), 133–148. http://dx.doi.org/10.1016/0301-9322(85)90041-2.

Krasnopolsky, B.I., Lukyanov, A.A., 2018. A conservative fully implicit algorithm for predicting slug flows. J. Comput. Phys. 355, 597–619. http://dx.doi.org/10.1016/j.jcp.2017.11.032.

Liao, J., Mei, R., Klausner, J.F., 2008. A study on the numerical stability of the two-fluid model near ill-posedness. Int. J. Multiph. Flow 34 (11), 1067–1087. http://dx.doi.org/10.1016/j.ijmultiphaseflow.2008.02.010.

Liou, M.-S., Nguyen, L., Chang, C.-H., Sushchikh, S., Nourgaliev, R., Theofanous, T., 2006. Hyperbolicity, discontinuities, and numerics of two-fluid models. In: Deconinck, H., Dick, E. (Eds.), Proceedings of the Fourth International Conference on Computational Fluid Dynamics. ICCFD4, Ghent, Belgium, pp. 625–630.

López de Bertodano, M., Fullmer, W., Clausse, A., Ransom, V.H., 2017. Two-Fluid Model Stability, Simulation and Chaos. Springer International Publishing, Cham, Switzerland, http://dx.doi.org/10.1007/978-3-319-44968-5.

Lyczkowski, R.W., Gidaspow, D., Solbrig, C.W., Hughes, E.D., 1978. Characteristics and stability analyses of transient one-dimensional two-phase flow equations and their finite difference approximations. Nucl. Sci. Eng. 66 (3), 378–396. http://dx.doi.org/10.13182/NSE78-4.

Montini, M., 2011. Closure Relations of the One-Dimensional Two-Fluid Model for the Simulation of Slug Flows (Ph.D. thesis). Imperial College London, United Kingdom.

Munkejord, S.T., 2006. Analysis of the Two-Fluid Model and the Drift-Flux Model for Numerical Calculation of Two-Phase Flow (Ph.D. thesis). Norwegian University of Science and Technology, Trondheim.

Prosperetti, A., Tryggvason, G., 2007. Computational Methods for Multiphase Flow. Cambridge University Press.

Ramshaw, J.D., Trapp, J.A., 1978. Characteristics, stability, and short-wavelength phenomena in two-phase flow equation systems. Nucl. Sci. Eng. 66, 93–102. http://dx.doi.org/10.13182/NSE78-A15191.

Remmerswaal, R.A., 2023. Numerical Modelling of Variability in Liquid Impacts (Ph.D. thesis). University of Groningen, The Netherlands, http://dx.doi.org/10.33612/diss.562133319.

Sanderse, B., Smith, I.E., Hendrix, M.H.W., 2017. Analysis of time integration methods for the compressible two-fluid model for pipe flow simulations. Int. J. Multiph. Flow 95, 155–174. http://dx.doi.org/10.1016/j.ijmultiphaseflow.2017.05.002.

Sanderse, B., Veldman, A.E.P., 2019. Constraint-consistent Runge–Kutta methods for one-dimensional incompressible multiphase flow. J. Comput. Phys. 384, 170–199. http://dx.doi.org/10.1016/j.jcp.2019.02.001.

Song, J.H., Ishii, M., 2001. On the stability of a one-dimensional two-fluid model. Nucl. Eng. Des. 204, 101–115. http://dx.doi.org/10.1016/S0029-5493(00)00253-3.

Stewart, H.B., Wendroff, B., 1984. Two-phase flow: Models and methods. J. Comput. Phys. 56 (3), 363–409. http://dx.doi.org/10.1016/0021-9991(84)90103-7.

Taitel, Y., Dukler, A.E., 1976. A model for predicting flow regime transitions in horizontal and near horizontal gas-liquid flow. AIChE J. 22 (1), 47–55. http://dx.doi.org/10.1002/aic.690220105.

Thorpe, S.A., 1969. Experiments on the instability of stratified shear flows: Immiscible fluids. J. Fluid Mech. 39 (1), 25–48. http://dx.doi.org/10.1017/S0022112069002023.

Toro, E.F., 1999. Riemann Solvers and Numerical Methods for Fluid Dynamics: A Practical Introduction. Springer, Berlin.

van Reeuwijk, M., 2011. A mimetic mass, momentum and energy conserving discretization for the shallow water equations. Comput. & Fluids 46 (1), 411–416. http://dx.doi.org/10.1016/j.compfluid.2011.01.006.

van 't Hof, B., Veldman, A.E.P., 2012. Mass, momentum and energy conserving (MaMEC) discretizations on general grids for the compressible Euler and shallow water equations. J. Comput. Phys. 231 (14), 4723–4744. http://dx.doi.org/10.1016/j.jcp.2012.03.005.

Veldman, A.E.P., 2021. Supraconservative finite-volume methods for the Euler equations of subsonic compressible flow. SIAM Rev. 63 (4), 756–779. http://dx.doi.org/10.1137/20M1317050.